https://doi.org/10.5194/egusphere-2025-1601
Preprint. Discussion started: 14 May 2025

How flat is flat? Investigating the spatial variability of snow surface temperature and roughness on landfast sea ice using UAVs in McMurdo Sound, Antarctica

Julia Martin[1,2], Ruzica Dadic[1,2], Brian Anderson[1], Roberta Pirazzini[3], Oliver Wigmore[1], and Lauren Vargo[1]

[1]Antarctic Research Centre, Victoria University of Wellington, Wellington, New Zealand
[2]WSL Institute for Snow and Avalanche Research SLF, Davos, Switzerland
[3]Finish Meteorological Institute FMI, Helsinki, Finland

Correspondence: Julia Martin (julia.martin@vuw.ac.nz)

Abstract. How do snow distribution patterns influence the surface temperature of snow on sea ice? Despite its crucial role in the sea-ice energy balance, snow on Antarctic sea ice remains under-sampled and poorly understood. To address this knowledge gap, we used an Uncrewed Aerial Vehicle (UAV) and ground measurements to produce a Digital Elevation Model (DEM) of the snow topography and a map of snow surface temperature over relatively uniform landfast sea ice (2.4 $\pm$ 0.04 m thick) in McMurdo Sound, Ross Sea, Antarctica during our field season in November-December 2022. A key methodological innovation in this study is an algorithm that corrects thermal drift caused by Non-Uniformity Correction (NUC) events in the DJI Matrice 30T thermal camera. The new algorithm minimizes temperature jumps in the imagery, ensuring consistent and accurate high-resolution (9 cm/px) snow surface temperature maps. Our airborne maps reveal a mean snow depth of 0.16 $\pm$ 0.06 m and a mean surface temperature of -14.7 $\pm$ 0.4 ℃. As expected, the largest surface temperature anomalies were associated with visible sediment depositions on the snow surface, which were manually identified. We found that the small-scale topography on a seemingly flat snow field significantly influences the incoming solar radiation (irradiance) at the point scale. Using a model that accounts for topographical effects on irradiance, we found that assuming uniform irradiance over our study (200x200 m) area underestimated irradiance variability due to relatively small-scale surface topography. The modeled mean irradiance, which accounts for surface topography is 592 $\pm$ 45 Wm^{-2} (1 Standard Deviation), whereas the mean measured irradiance at the point scale is 593 $\pm$ 20 Wm^{-2}. This shows that assuming a flat surface fails to represent the full irradiance range and may impact non-linear energy balance processes. While we initially hypothesized that snow depth was a key driver of snow surface temperature, our results indicate that sediment deposition and irradiance exert a far greater influence, overriding the effect of snow depth for this test site. Our results improve our understanding of snow's spatial distribution, how it influences snow surface temperatures and how it may influence the sea-ice energy balance.

.

https://doi.org/10.5194/egusphere-2025-1601
Preprint. Discussion started: 14 May 2025

1 Introduction

The effects of climate change have far-reaching consequences in polar environments, particularly in the ice-dominated high-latitude regions of the Arctic and Antarctica (Callaghan et al., 2011; Simmonds, 2015; Lindsay and Schweiger, 2015; Meredith et al., 2022). These regions experience polar amplification, a phenomenon where warming is more pronounced compared to lower latitudes (Stuecker et al., 2018). As polar ice caps, glaciers, and sea ice melt, the exposed darker surfaces, such as the open ocean and bare land surfaces, can absorb more solar energy, leading to further increases in melting and darkening. These changes in the ice-albedo feedback lead to more warming and influence large-scale atmospheric circulation patterns (Perovich et al., 2007).

Sea ice growth and decay play a key role in this ice-albedo feedback loop (Riihelä et al., 2021). The annual growth cycle of sea ice is one of the most extensive changes observed on Earth's surface (Parkinson, 2014), and its long-term trend differs significantly between the Arctic and Antarctica. Arctic sea ice has experienced a trend of rapid sea ice loss (Lindsay and Schweiger, 2015). In contrast, the minimum Antarctic sea ice extent exhibits more variability, with a general increase through the satellite period until 2016, and a decrease thereafter. Recent records show the lowest minimum extent since record-keeping began (Wang et al., 2022). The thickness, extent, and duration of sea ice impact the absorption and reflectance of solar radiation, thereby influencing the Earth's energy balance (Massom and Stammerjohn, 2010). Additionally, sea ice affects ocean circulation patterns, ecosystems, and the carbon cycle (Stein et al., 2020; Massom and Stammerjohn, 2010).

Snow cover is a critical factor in sea ice thermodynamics, impacting interactions between sea ice and the atmosphere (Landrum and Holland, 2022). Snow, one of the most insulating natural materials, is a barrier to heat exchange between the ocean, sea ice, and atmosphere (Webster et al., 2018). It also has a high albedo, up to 0.9, compared to the albedo of bare sea ice (∼0.4-0.6) or the open ocean (0.06) (Perovich et al., 2007; Brandt et al., 2011; Light et al., 2022; Smith et al., 2022), enhancing reflectance and influencing regional and global climate by affecting heat and mass balance (Zatko and Warren, 2015). Snow accumulation and metamorphism impact the conductive and radiative properties of sea ice, affecting its thickness, salinity, temperature, and permeability, highlighting the importance of understanding snowpack dynamics (Sturm et al., 1997; Perovich and Polashenski, 2012). For these reasons, our original hypothesis was that snow surface temperatures over sea ice with relatively uniform thickness would strongly correlate with snow depth, because of snow's high albedo and low thermal conductivity.

Snow on sea ice research is predominantly focused on Arctic conditions, with the Multidisciplinary Drifting Observatory for the Study of Arctic Climate (MOSAiC) providing substantial insights into the sea-ice system, including snow (Nicolaus et al., 2022; Macfarlane et al., 2023). However, Antarctic snow on sea ice differs markedly from its Arctic counterpart, with large spatial variability depending on the location. Antarctic snow is generally thicker (Arndt et al., 2017; Arndt and Paul, 2018; Nicolaus et al., 2021; Lawrence et al., 2024) colder, and persists throughout the year, contrasting with the thinner, warmer snow in the Arctic (Massom et al., 2001). In McMurdo Sound, snow on sea ice persists through summer until breakout, but is generally thinner than in other Antarctic fast ice regions (Brett et al., 2020). This persistent snow cover

https://doi.org/10.5194/egusphere-2025-1601
Preprint. Discussion started: 14 May 2025

influences sea ice albedo, primarily through snow thickness and physical properties such as specific surface area, salinity and liquid water content in summer (Zhou et al., 2001). In some areas in Antarctica, like the Weddel Sea, the thick snow cover and thinner sea ice lead to flooding, where the weight of the snow depresses the ice surface, allowing seawater to infiltrate the snow. This seawater-saturated snow then refreezes, resulting in snow-ice formation and thickening of the ice from above (Eicken et al., 1994; Massom et al., 2001; Arndt et al., 2017).

Despite the critical role of snow on sea ice dynamics, there is a significant knowledge gap regarding Antarctic snow properties. Comprehensive datasets are notably limited, especially concerning the spatial evolution of snow on sea ice (Eicken et al., 1994; Massom et al., 2001; Brandt et al., 2005; Sturm and Massom, 2016; Arndt and Paul, 2018). In McMurdo Sound, for example, research is sparse and fragmented (Price et al., 2013, 2019; Brett et al., 2020). Recent advancements, such as the Tan et al. (2021) airborne study provide valuable data into snow depth distribution, but underscore the need for more extensive datasets to address critical gaps in our understanding of Antarctic snow on sea ice dynamics. The lack of comprehensive snow data on Antarctica sea ice, and the significant differences between the Antarctic and Arctic lead to biases in modeling sea ice behavior and errors in global climate system scenarios (Wever et al., 2021; Landrum and Holland, 2022).

To collect data on the physical properties of snow on Antarctic sea ice, drones are a promising tool (Gaffey and Bhardwaj, 2020; Pirazzini et al., 2021; Román et al., 2024). They have been widely used in scientific studies of the cryosphere outside the polar regions (Buhler et al., 2016; Sproles et al., 2020). Drones can cover extensive areas and simultaneously measure certain snow parameters at very high resolution, bridging the gap between point-based ground measurements and low-resolution satellite remote sensing (Wigmore et al., 2019; Tan et al., 2021; Wigmore and Molotch, 2023), and even provide opportunities for validating satellite remote sensing products. For example, airborne laser scanning has been used to assess ICESat-2's ability to capture sea ice surface topography and roughness, revealing limitations in detecting small-scale features such as ridges and cracks (Ricker et al., 2023). Similarly, drone-based observations could contribute to validating missions like PREFIRE (Kahn et al., 2020), which aims to improve our understanding of the Earth's energy budget in polar regions.

Our study has two primary objectives: **(1) To quantify the spatial variability of snow cover on landfast, flat sea ice and test our hypothesis that snow thickness (which affects albedo and thermal resistance) determines snow surface temperatures and energy balance of the sea ice system, over relatively uniform sea ice.** To achieve this first objective, we required a high-resolution dataset capable of capturing and quantifying the variability across different scales. Thus, **(2) we aimed to develop and validate a method of accurately mapping snow surface topography and surface temperature on flat sea ice in the polar regions.** We used multi-spectral (visible, infrared) UAV imagery at sub-metre spatial resolution, closely following the workflow published by Wigmore et al. (2019). To achieve this, we integrate airborne surface elevation and temperature data collected in November 2022 with ground-based surveys of snow depth, snow surface temperature, and ice thickness. The datasets from objective (2), combined with topography-dependent irradiance modeling, allowed us to examine how snow cover depth influences snow surface temperatures. While our extensive dataset did not confirm our relatively simple hypothesis, highlighting once again the complexity of

https://doi.org/10.5194/egusphere-2025-1601
Preprint. Discussion started: 14 May 2025

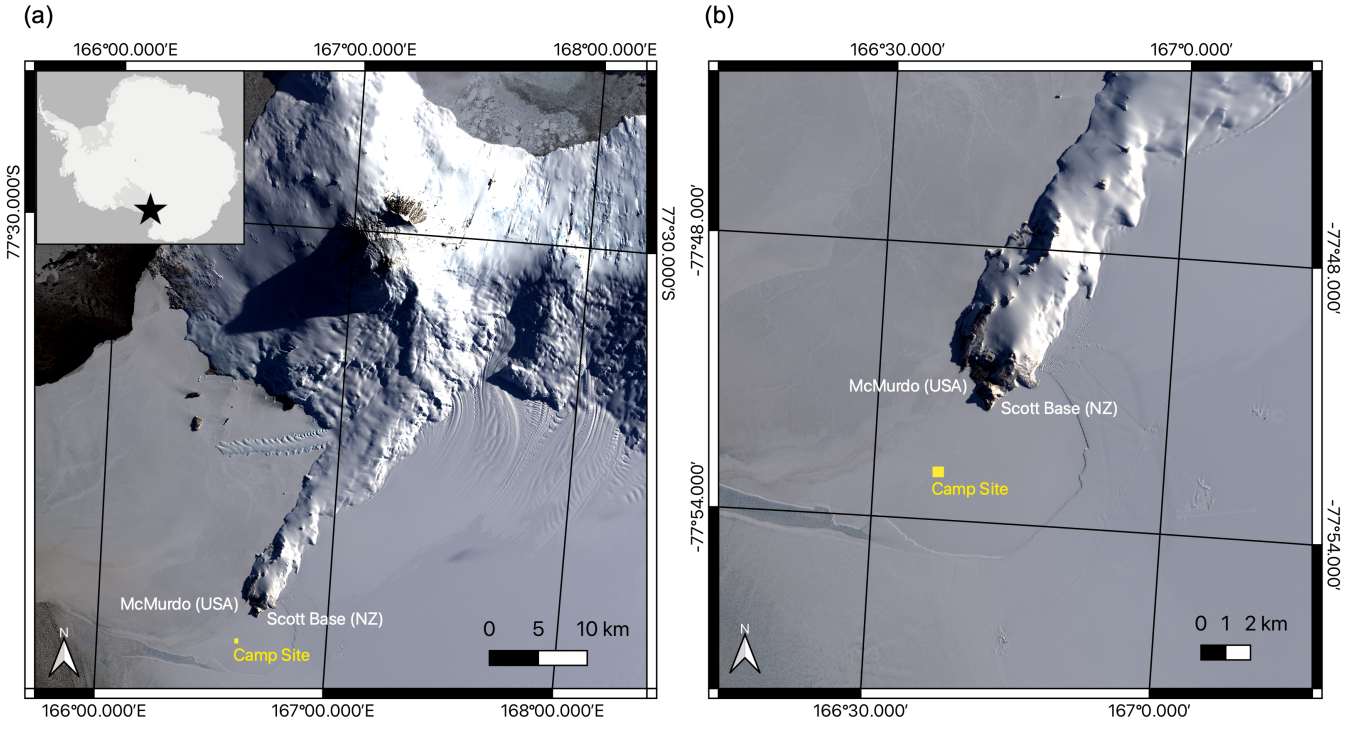

Figure 1. Landsat image from November 6, 2022. (a) Study area (black star) in West Antarctica, McMurdo Sound, and Ross Island with Scott Base (NZ), McMurdo Station (USA), and the Camp Site (CS) test field(yellow rectangle). (b) CS location on the ice wedge between the Ross Ice Shelf and the tip of Ross Island.

snow on sea ice, our research provides new insights into how small-scale surface roughness affects the sea ice's energy balance. Moreover, it offers a novel, much-needed snow dataset aimed at improving climate model accuracy.

2 Methods

During a field campaign in November 2022 (4 weeks), we collected snow and sea ice data on the fast ice in front of the McMurdo Ice Shelf, Ross Sea, about 5 km southwest of Scott Base and McMurdo Station. We collected a new and unique airborne dataset consisting of aerial Red, Green, Blue (RGB) and Thermal InfraRed (TIR) images of the snow surface along with photogrammetrically derived digital elevation models; which we validated and correlated with ground-based surface temperature, snow depth, and ice thickness surveys.

2.1 Study site and conditions

McMurdo Sound is located in West Antarctica, in the southwestern part of the Ross Sea, framed by Ross Island to the east, the Ross Ice Shelf to the south, and Victoria Land to the west (Fig. 1a). McMurdo Sound has a variable snow

https://doi.org/10.5194/egusphere-2025-1601
Preprint. Discussion started: 14 May 2025

cover of 0.1 – 0.3 m (Brett et al., 2020) and limited snow-ice formation compared to wetter regions like the Weddell Sea (Maksym and Markus, 2008). The landfast sea ice is usually 2 – 2.5 m thick (Brett et al., 2020), and there is an extensive sub-ice platelet layer (up to 9 m) due to the proximity of the Ross Ice Shelf and its super-cooled water supply (Gough et al., 2012; Langhorne et al., 2015; Haas et al., 2021). During our field campaign, the average wind speed was 4.7 ms^{-1}, and the average temperature was -14.2 ℃ (Fig. A1).

Usually, sea ice formation starts in March and lasts until October, followed by a break-out in January/February. In 2022, the sea ice formation was highly impacted by southerly storms repeatedly interrupting the sea ice formation cycle, similar to the conditions in winter 2019 (Leonard et al., 2021). Except for a small "wedge" of ice pinned between the front of the ice shelf and the tip of Ross Island (Fig. 1b), the Sound remained largely ice-free until August 2022. As a result, two distinct sea ice types formed: "old ice", which began forming in the typical cycle around March/April and reached a thickness of about 2.5 m during our field campaign, and "new ice", which started forming only after August 2022 and grew to about 1-1.5 m thickness by November 2022. During the November 2022 field campaign, we collected data on five 200x200 m sites with different snow and ice conditions, of which we only discuss one in this study. The data in this paper were collected at our main test site (Camp Site; CS), a 200x200 m area located on the flat "old ice", during November 2022 (Fig. 1b, yellow rectangle). The other four sites are outside the scope of this paper and we will present them in a follow-up study, which will focus less on the techniques and more on the differences between the sites.

2.2 Ground-based data

Our ground-based dataset consists of automated radiation data, weather data, and snow and ice depth measurements. All sensors, instruments and parameters used in this study are listed in Table 1.

2.2.1 Radiation and weather data

We installed automated measurement stations to capture the local radiation, surface temperature, and weather conditions and validate and correct the airborne measurements. The radiation station was outfitted with a pair of Kipp&Zonen CMP22 pyranometers, one facing upward and one facing downward, to measure the broadband incident (Sw↓) and reflected (Sw↑) solar irradiance in the 200-3600 nm wavelength range, and a pair of Kipp&Zonen CGR4 pyrgeometers, one facing upward and one facing downward, to measure the broadband incoming (Lw↓) and outgoing (Lw↑) longwave radiation in the 4500-42000 nm wavelength range. The sensors were ventilated, and according to the manufacturer's specifications, the nominal accuracy of the Sw and Lw measurements is 1% and 3%, respectively. The radiation station also included a DeltaT SPN1 radiometer that measured broadband global and diffuse incident irradiance (Sw↓ and $Sw_{diff}\downarrow$) in the 400-2700 nm wavelength range. According to the manufacturer, the nominal accuracy of both measurements is $\pm$ 8 %. Inter-calibration studies have shown that an extra factor of 1.05 should be applied to $Sw_{diff}\downarrow$ to compensate for its systematic underestimation (Badosa et al., 2014). A stationary Apogee infrared radiometer (model SI-121-SS) installed slightly north of the radiation station was pointing at clean snow ("cold target") with an angle of approximately 45 ° mounted at 1.2 m height, leading to an elliptical footprint of about 1.6 m^2. The data were logged every 10 s. A non-stationary Apogee

https://doi.org/10.5194/egusphere-2025-1601
Preprint. Discussion started: 14 May 2025

Table 1. Summary of ground-based and airborne instruments with measurement parameters and uncertainties used in this paper. The uncertainty for the airborne snow depth (*) is the propagated error counting for the magnaprobe snow depth error and the GCP error in the z-direction.

Airborne	Ground-based	Parameter	Instrument/Method	Unit	Uncertainty
	x	Ice Thickness	Geonics EM31	m	± 0.1
	x	Snow Depth	SnowHydro magnaprobe	m	± 0.01
x		Snow Depth (Proxy)	DJI Matrice 30T	m	± 0.05*
	x	Surface Temperature	Apogee SI-121-SS	℃	± 0.2
x		Surface Temperature	DJI Matrice 30T	℃	± 2
	x	Wind Direction	R.M. Young Heavy Duty Wind Monitor HD-Alpine	°	± 3
	x	Wind Speed	R.M. Young Heavy Duty Wind Monitor HD-Alpine	ms^{-1}	± 0.3
	x	Air Temperature	Vaisala HMP155 Temperature Probe	℃	± (0.226 - 0.0028 × temperature)
	x	Relative Humidity	Vaisala HMP155 Temperature Probe	%	± 2%
	x	Incoming/Outgoing Shortwave Radiation	Kipp & Zonen CMP22 Pyranometer	Wm^{-2}	± 1.2% to ± 1.4%
	x	Incoming/Outgoing Longwave Radiation	Kipp & Zonen CGR4 Pyrgeometer	Wm^{-2}	± 1.5% to ± 2.0%
	x	Location (Long/Lat)	Septentrio AsteRx	m	± 0.01 horizontally ± 0.02 vertically

infrared radiometer (model SI-121-SS) on a tripod was placed in the test field. It pointed at a sediment patch ("sediment target") mounted at 1.02 m, with a footprint of 0.35 m^2. We collected meteorological data (wind speed, air temperature, precipitation and relative humidity) with an automated weather station (AWS) at 10-minute intervals.

2.2.2 Snow depth

To capture the spatial distribution of snow depth, we conducted magnaprobe transects (Sturm and Holmgren, 2018). The magnaprobe is a user-friendly device that allows for rapid snow depth measurements. The snow depth is measured by inserting a 1.53 m steel rod with a sliding ring magnet inside a plastic disk into the snow until the tip of the rod hits the ground. An electronic pulse from a magnetostrictive sensor determines the position of the magnet, converting the signal into the distance from the rod's tip to the disk and indicating snow depth. The snow depth and the GPS position (GARMIN™ receiver and Campbell Scientific antenna) are recorded with a Campbell Scientific CR800 data logger Sturm and Holmgren (2018). The accuracy of the snow depth depends on (1) the hardness of the underlying surface (a too-soft material will cause compaction and over-probing), (2) the positioning of the plastic disk on the snow surface and (3) the

https://doi.org/10.5194/egusphere-2025-1601
Preprint. Discussion started: 14 May 2025

correctness of the vertical angle. For our measurement campaign, the uncertainty is mainly influenced by (2) and (3) as the snow surface is relatively hard and uneven, affecting the insertion of the probe and the ability of the plastic disk to lie flat on the snow surface. We assume the measurements are within a $\pm$ 0.02 m uncertainty, which is slightly larger than the 0.01 m assumed for the winter MOSAiC measurements over likely similar roughness (Itkin et al., 2023). The GPS accuracy is $\pm$ 2.5 m. Our measurement strategy was to conduct transects along the measurement field borders and a cross through the middle, taking a measurement approximately every meter, which resulted in 813 measurements for this particular "study field".

2.2.3 Ice thickness

We used the Geonics electromagnetic conductivity meter (EM31) combined with manual drilling to survey the ice thickness. The EM31 is a geophysical instrument that measures sea ice conductivity and in-phase components to detect subsurface features (Tateyama et al., 2006). It operates based on the principles of electromagnetic induction. The EM31, consisting of a transmitter and receiver coil, was mounted on a sledge and towed over the snow by a snow machine. The transmitter coil emits a primary electromagnetic field into the ground, and as the field penetrates the ice, it reaches the conductive seawater beneath. This causes strong eddy currents to form, generating a secondary electromagnetic field. The receiver coil detects this secondary field, which is altered by the distance it travels through the ice. The EM31 measures the apparent conductivity of the subsurface and the phase shift between the primary and secondary fields. These measurements are recorded continuously as the instrument is moved across the ice. To account for local variations in ice thickness and device calibration, we took direct ice thickness measurements at various points (approximately every 50 m) using a Covacs ice drill. We used the same survey pattern for the EM31 ice thickness measurements as for snow depth. While there is a significant platelet ice layer in our survey field, we excluded it from our ice thickness evaluation by calibrating the EM31-signal to ice and snow thickness only. The snow and ice thickness was calculated following a linear regression between conductivity and manually measured ice and snow thickness at the CS test field:

$$h_{ice+snow} = -0.0103 * \kappa + 4.2285 \quad (1)$$

with $h_{ice+snow}$ the combined ice and snow thickness and κ the conductivity. During our surveys the EM31 was mounted 0.5 m above the surface (snow or ice depending on the measurement location) on a sledge that was pulled with a snow machine. To calculate only the ice thickness, we subtracted the sledge height as well as the average snow depth of 0.16 m (Fig. 11a).

2.3 Airborne data

We used a DJI Matrice 30T, a multi-rotor (quadcopter) UAV with self-heating batteries, suitable for operations in polar conditions (temperature range from -20 to +50 ℃). The UAV has a wide-angle camera (12 megapixels) for RGB images and a thermal camera (Uncooled Vox Microbolometer, long-wave infrared spectrum 8-14 μm, 1.31 megapixels) for TIR

https://doi.org/10.5194/egusphere-2025-1601
Preprint. Discussion started: 14 May 2025

images with an accuracy of ± 2 ℃ or ±2 % (Da Jiang Innvoations (DJI), 2022). The exact wavelength for the wide angle and TIR camera is unknown.

To retrieve RGB and TIR imagery, we programmed two missions following a lawnmower cross-grid survey pattern at two different flight altitudes, and executed them on November 14, 2022. The first flight at 60 m altitude took off at 22:12:00 and finished at 22:31:19 (UTC). We changed the batteries and executed the second flight at 75 m altitude, with the take-off at 22:44:45 and landing at 23:01:37 (UTC). The frontal overlap of the images was set to the maximum of 95 % and the side overlap to 80 %. The high frontal overlap only affects the frequency at which the pictures are taken and does not affect the flight pattern or flight time. The RGB and TIR images were shot simultaneously.

2.3.1 Georeferencing

To georeference the RGB and TIR images, we used 10 targets as Ground Control Points (GCPs) on the snow surface across the 200x200 m measurement area before the drone flight. The RGB targets were 0.3x0.3 m sheets of yellow coroplast plastic, with a pink duct-tape cross defining a centre point. For the TIR survey, 0.4x0.4 m black targets were installed next to the RGB targets. As back (hot) targets, we used thermal insulation material, similar to camping mats, that was black on the top side, with silver-colored foil as backing (similar to first aid blankets) at the bottom. The location of each of the RGB targets was measured using dual-frequency GNSS receivers, and post-processing was done using the Precise Point Positioning kinematic method (Malinowski and Kwiecień, 2016) and the software «teqc»(Estey and Meertens, 1999).

2.3.2 Digital Elevation Model (DEM)

We derived the DEM from the RGB images following the workflow detailed in Fig. 3. First, we generated the sparse point cloud through image alignment and tie-point generation. After georeferencing using GCPs from both RGB and TIR images, we optimized the sparse cloud by removing outliers with poor accuracy values. We then created a dense point cloud, generated a triangular irregular network (TIN) mesh and finally calculated the RGB orthomosaic (2 cm/px ground resolution) and DEM (5 cm/px ground resolution). We upscaled both to 9 cm/px to match the TIR orthomosaic resolution. The projection error for the RGB orthomosaic and DEM is 0.96 px, and the GCP errors in x, y, and z directions are 0.05 m, 0.05 m and 0.04 m.

As the last processing step, we detrended the DEM by fitting a planar surface to the elevation data and subtracting this fitted plane from the original DEM. The trend is likely due to the time window of about 3 hours between when the GCP survey was conducted and when the site was flown, as the site is influenced by tidal variations, which are about 0.2 m for this 3-hour time window as shown in Fig. A4. We fitted a plane through the DEM to remove this trend, determined the best-fit parameters for the plane, and subtracted it from the original DEM, producing a detrended DEM. This allowed us to focus on analyzing the smaller-scale topographical features of the snow surface, which is the aim of this study.

https://doi.org/10.5194/egusphere-2025-1601
Preprint. Discussion started: 14 May 2025

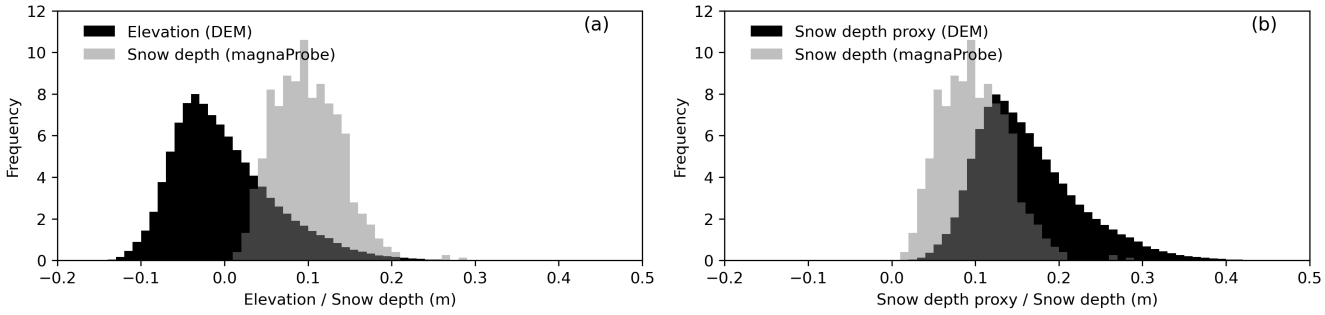

Figure 2. (a) Histogram representing an estimate of the Probability Density Function (PDF) of the elevation in m from the DEM and the snow depth in m from the magnaprobe transect. The offset between the minimum elevation value and minimum snow depth value is at 0.16 m. (b) Histogram (PDF) of the offset corrected DEM elevation in m (now: snow depth proxy) and the snow depth in m from the magnaprobe transect.

2.3.3 Snow depth proxy

Mapping snow depth typically requires surveying the area both when it is snow-free and when it is snow-covered. However, this approach was not feasible in our case because the underlying surface is sea ice, which was never snow-free (for our field work window) and continuously changed in elevation due to tides, thickening, and thinning processes. To address this challenge, we developed an alternative method (Fig. 2) to approximate snow depth using the detrended DEM (Fig. 8b). Without a bare-ground Digital Terrain Model (DTM), we assumed the underlying sea ice surface was flat and smooth (Fig. 7, A1), and we interpreted the DEM elevations as representing the snow surface topography. To calculate a snow depth proxy, we applied a single value offset correction based on the ground-based magnaprobe measurements to correct the differences between DEM elevation and actual snow depth (Fig. 2a). The offset (0.16 m) was calculated as the difference between the minimum magnaprobe snow depth value (0.012 m) and the minimum DEM elevation value (-0.149 m, Fig. 2a). The 0.16 m offset was added to the DEM elevation to calculate a snow depth proxy for each pixel, as shown in Fig. 2b. While the magnaprobe measurements (with a snow depth error of $\pm$ 0.02 m) provided a valuable correction, the resulting values remain a proxy rather than exact snow depths. A key limitation is that the magnaprobe locations were not surveyed with high-accuracy GNSS, preventing a precise validation of our approach. As a workaround, we relied on the assumption of a smooth ice surface, which is supported by field observations (Fig. A1) but does not account for potential localized roughness variations that were not sampled. Additionally, an estimated vertical uncertainty of $\pm$0.04 m from ground control points (GCPs) results in a total propagated error of approximately $\pm$0.05 m for the snow depth proxy.

https://doi.org/10.5194/egusphere-2025-1601
Preprint. Discussion started: 14 May 2025

2.3.4 TIR image processing: File conversion RJPEG to TIFF

The first step is to convert the TIR images from the proprietary Radiometric JPEG (RJPG) format, primarily used by thermal sensors (e.g. FLIR), to Tagged Image File Format (TIFF) using the ImageJ IR UAV plugin (Pereyra Irujo, 2022). This conversion is necessary because the RJPG format retains absolute brightness temperature values in degrees Celsius but does not support temperature extraction and analysis in its native form. For the conversion from RJPG to TIFF with the ImageJ IR UAV plugin, we used the following input parameters: reflected surface (snow) temperature -13.2 °C, relative humidity 65.2 % based on our automated measurements from the AWS during the flight time, an object (snow) emissivity of 0.98 and an object distance of 25 m. The exact values of these parameters are not critical because we calibrate the brightness temperatures with ground surface temperature measurements. However, these initial parameters are needed for the file format conversion. After that initial step, all data was processed using the SfM workflow implemented in Agisoft Metashape Pro version 1.8.4 (build 14856, 64-bit). Our workflow is closely aligned with Wigmore and Molotch (2023), with processing details described in Fig. 3.

2.3.5 TIR image processing: Non-Uniformity Correction (NUC)

The thermal camera of the DJI Matrice 30T uses an uncooled microbolometer, which is prone to non-uniformities in its sensor array; each pixel responds slightly differently to the same temperature. To correct for measurement drift caused by these differences, the camera performs periodic internal calibrations known as Non-Uniformity Correction (NUC) events. This process involves a shutter that blocks the lens, providing a uniform temperature source for calibration. The camera measures each pixel's response to this source and adjusts its settings to correct any discrepancies. After calibration, these adjustments ensure accuracy and uniformity in subsequent images. The frequency of NUC events varies depending on the camera model and environmental conditions, but it is often not documented and seldom adjustable for off-the-shelf drones, like the DJI Matrice 30T. Consequently, temperature differences of up to 1.5 °C can occur in consecutive TIR images taken before and after a NUC event, as shown in Fig. 4a (red and yellow dots, respectively).

We present a novel algorithm to correct for temperature discrepancies caused by NUC events based on the steps listed below.

Step 1: Read sequential image pairs (RJPG; 1280x1024 px)

Step 2: Identify overlapping areas in each image pair (in this dataset, the overlap is at least 70 %). We do this by finding and extracting unique features to ensure identical regions in each image pair. For this, we use the Oriented FAST and Rotated BRIEF (ORB algorithm) detector, which combines two key components: FAST (Features from Accelerated Segment Test) and BRIEF (Binary Robust Independent Elementary Features Descriptor). FAST identifies interesting points (corners) in an image, similar to spotting unique landmarks on a city map. BRIEF then describes these corners using compact binary "fingerprints," analogous to noting a landmark's distinctive features (e.g., "a red brick house with a tall chimney"). The ORB algorithm enables efficient and robust feature matching between images (Rublee et al., 2011; Bradski, 2000). Then, we use the Brute-Force Matcher (Bradski, 2000) to calculate

https://doi.org/10.5194/egusphere-2025-1601
Preprint. Discussion started: 14 May 2025

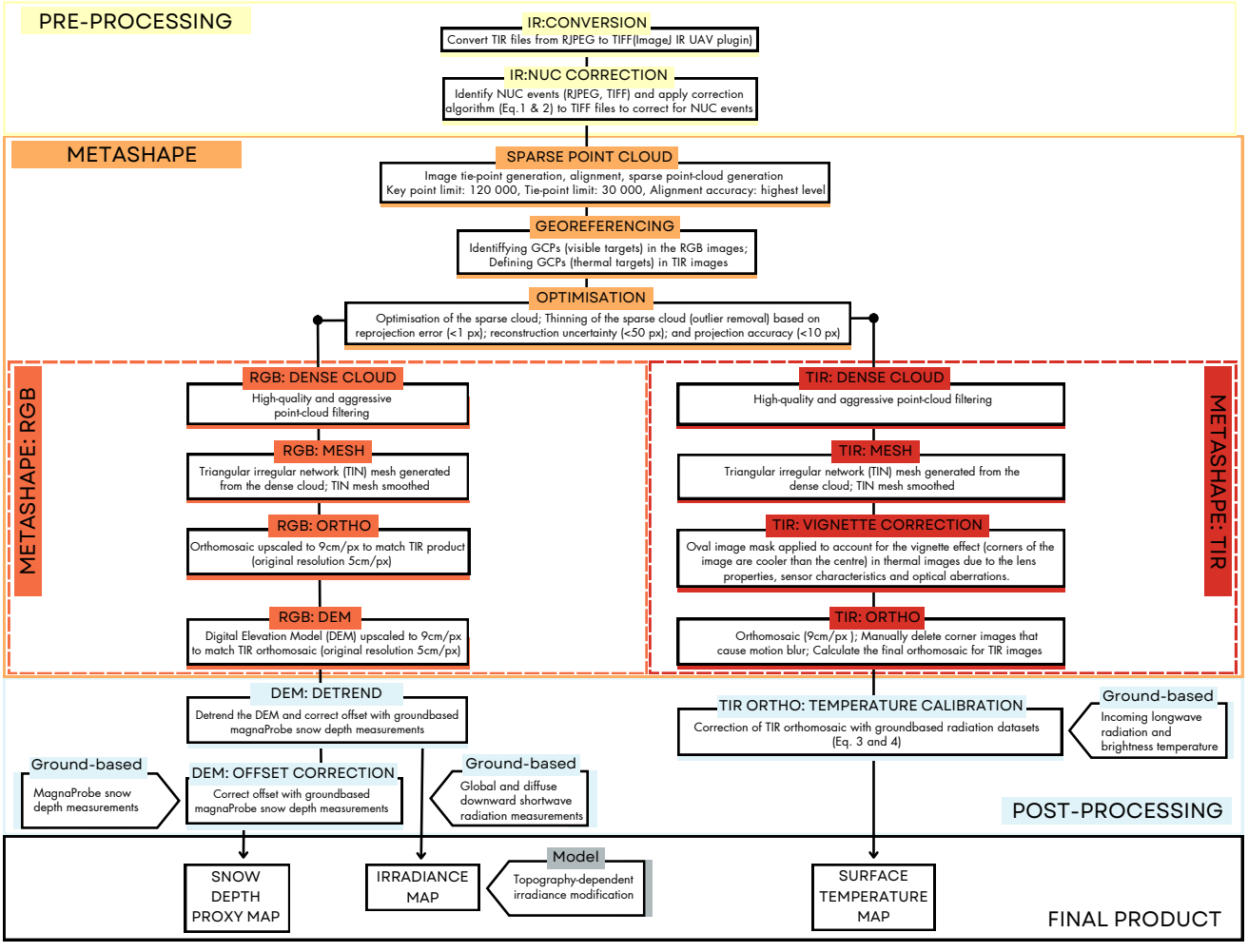

Figure 3. Workflow for processing and analyzing RGB and TIR images captured with the DJI Matrice 30T during two flights in 60 and 75 m altitude. The process includes converting RJPG images to TIFF format using the ImageJ IR UAV plugin, applying the NUC correction algorithms for the internal camera calibration, and processing both TIR and RGB images through photogrammetry steps in Metashape. Key steps include sparse point-cloud generation, georeferencing, optimization, dense cloud generation, mesh creation and the DEM and RGB/TIR orthomosaic production. Then, we apply a final offset correction using ground-based magnaprobe snow depth measurements and the surface temperature calibration using ground-based Apogee temperature data.

https://doi.org/10.5194/egusphere-2025-1601
Preprint. Discussion started: 14 May 2025

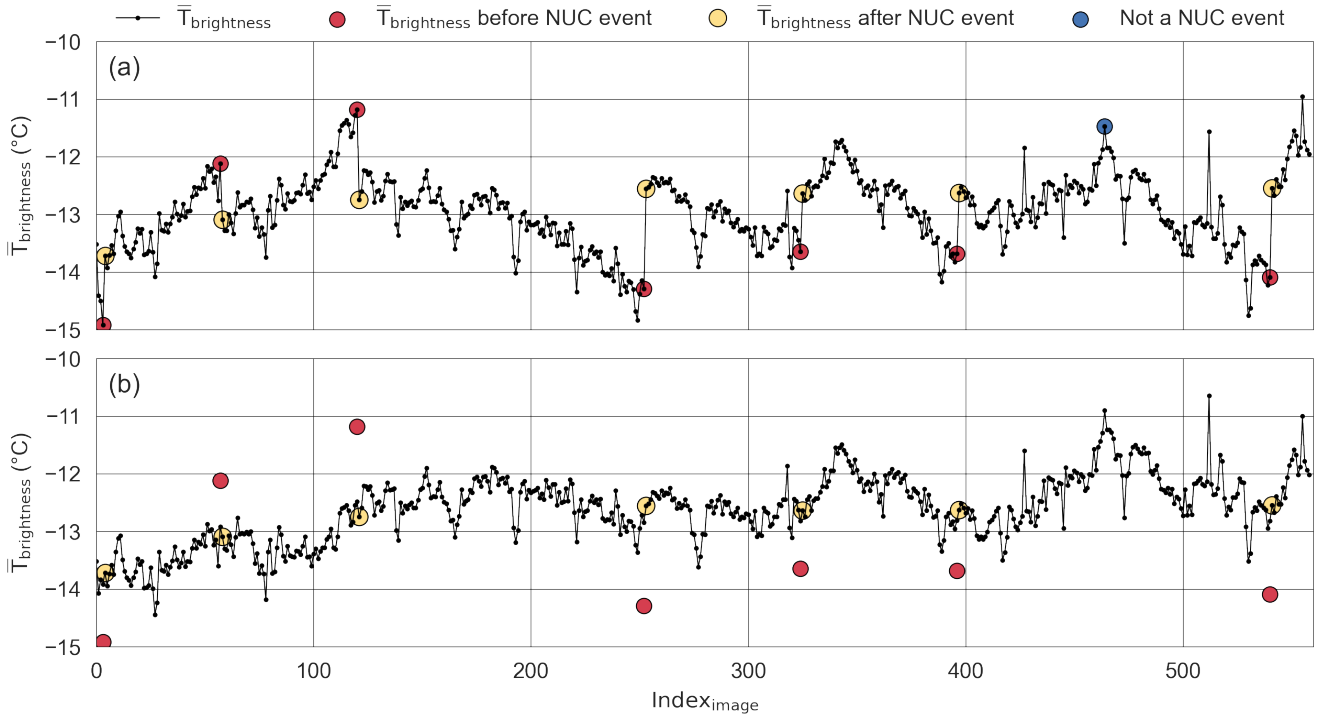

Figure 4. Illustration of NUC events (a) and their correction (b) for the first flights at 60 m altitude. (a) Mean brightness temperature ($\overline{T}_{brightness}$) for overlap area per image. Red dots indicate $\overline{T}_{brightness}$ before the NUC event, and yellow dots indicate $\overline{T}_{brightness}$ after the NUC event. NUC events are temperature jumps of more than 0.5 °C in two consecutive images. The blue dot indicates a temperature outlier for one image, which is not a NUC event. (b) The same dataset after the correction algorithm (Eq. 2 and Eq. 3) is applied.

corresponding points and select the 50 best feature matches in each image pair to estimate a homography matrix, which describes the geometric relationship between the two images.

Step 3: For each pair of successive images, the first image is warped to align with the grid of the second image to ensure accurate overlap and compensate for camera movement.

Step 4: Extraction of brightness temperatures from each pixel. From here on, we use the converted TIFF images (TIFF; 640x512 px).

Step 5: For each TIFF image, calculation of the mean brightness temperature $\overline{T}_{brightness}$ of the area overlapping with the following image. Ideally, the $\overline{T}_{brightness}$ of the same overlapping area in different images should match, as the thermal images were captured nearly simultaneously. However, due to temperature drift and NUC events, discrepancies arise and must be corrected.

https://doi.org/10.5194/egusphere-2025-1601
Preprint. Discussion started: 14 May 2025

Step 6: Identification of NUC events. A NUC_i event, with $i = 1,...m$ (m being the total number of NUC events during the considered flight), is identified when the absolute differences between the $\overline{T}_{brightness}$ of overlap regions in consecutive images is > 0.5 ℃ (Fig. 4a). Between two NUC events, NUC_i and NUC_{i+1} there are n images I_j, with $j = 1,...n$ (n being the number of TIR images taken between two consecutive NUC events). For image I_j, $\overline{T}_{brightness(i,j)}$ represents the mean temperature of image I_{j+1} (in the overlap region). We do not consider a temperature change $> \pm$ 0.5 ℃ to be a NUC event if it affects one image only (e.g. Fig. 4a: blue dot).

Step 7: Correction of the temperature drift between two consecutive NUC events. We assume that the temperatures measured immediately after the NUC events are accurate, and that the temperature drift (drift rate d_i) over the n images between two consecutive NUC events (NUC_i and NUC_{i+1}) is linear:

$$d_i = (\overline{T}_{brightness(i+1,1)} - \overline{T}_{brightness(i,n)})/n \quad (2)$$

where $\overline{T}_{brightness(i,n)}$ is the mean temperature of the overlap area in the final image n in the series after the NUC_i event (red dots in Fig. 4), and $\overline{T}_{brightness(i+1,1)}$ is the mean temperature of the overlap area in the first image after the NUC_{i+1} event (yellow dots in Fig. 4). d_i is then applied to calculate the linear correction $c_{i,j}$ for the $\overline{T}_{birghtness(i,j)}$ mean temperatures of the $j = 1,...n$ images between NUC_i and NUC_{i+1}:

$$c_{i,j} = j * d_i \quad (3)$$

The brightness temperature of each pixel in each TIR image is then corrected by adding $c_{i,j}$.

To understand the improvement achieved with this temperature correction procedure, we analysed the temperature in 250 random areas of 10x10 m^2 taken from the NUC uncorrected and NUC corrected TIR orthomosaics. While the NUC correction algorithm is applied sequentially (it depends on the order of images), we found that this analysis does not depend on the order in which the images were taken. For each of the 250 areas that contained at least 10 images, we calculated the temperature anomaly per image by subtracting the mean areal temperature from the mean image temperature $\overline{T}_{brightness}$. By comparing the temperature anomalies in the NUC uncorrected and NUC corrected TIR orthomosaic, we can assess the algorithm's impact performance in reducing drift and variability of temperature anomalies (Fig. 5a, dark grey vs. light grey) across the dataset.

In the NUC uncorrected TIR orthomosaic, the spread of anomalies ranged between $\pm$ 4 ℃ due to the temperature drift in between NUC events and the consequent variability in $\overline{T}_{brightness}$ among the images capturing the same overlapping area. In the NUC corrected TIR orthomosaic, the distribution of temperature anomalies narrowed to the range $\pm$ 2 ℃, there were fewer outliers, and the whiskers of the temperature anomaly boxplot shrank (Fig. 5a and b). This suggests that our correction improved the repeatability of $\overline{T}_{brightness}$ at each site, reaching an accuracy comparable to the sensor

https://doi.org/10.5194/egusphere-2025-1601
Preprint. Discussion started: 14 May 2025

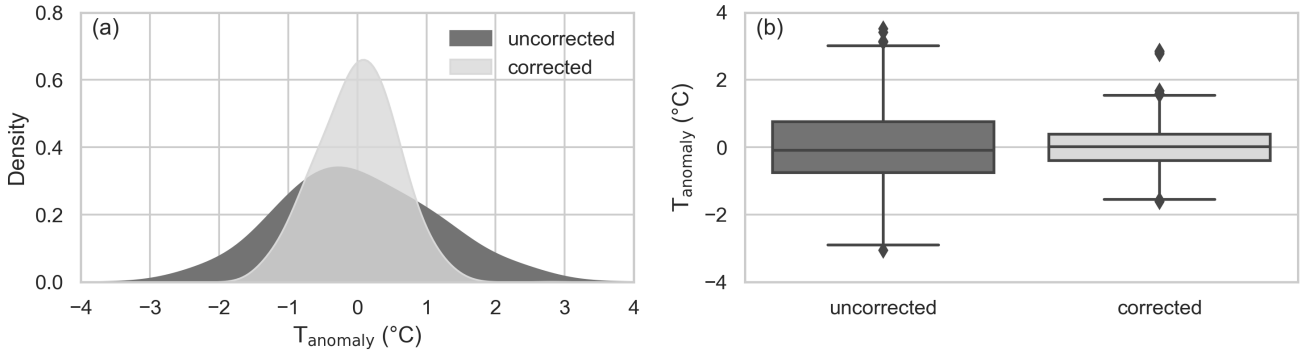

Figure 5. (a) The Kernel Density Estimate (KDE) function and boxplots (b) showing the distribution of brightness temperature anomalies in the 250 randomly sampled areas of 10x10 m^2 taken from the NUC uncorrected (dark grey) and NUC corrected (light grey) TIR orthomosaics.

uncertainty (see Sect. 2.3. The Root Mean Square (RMSE) of the temperature anomalies across all 250 sampled areas was 1.11 ℃ in the NUC uncorrected orthomosaic and decreased by 0.53 ℃ in the NUC corrected orthomosaic.

2.3.6 TIR orthomosaic

To produce the TIR orthomosaic, we first generated the sparse point cloud through tie-point generation, alignment, and cloud creation. After georeferencing with GCPs from both RGB and TIR images, we optimized the sparse cloud by removing outliers. We then created a high-quality, dense point cloud, generated a TIN mesh, and applied a vignette correction mask. The vignette correction mask is applied to account for the temperature distortion at the edges (corners) of the TIR images, which tend to be cooler than the centre due to lens properties, sensor characteristics, and optical aberrations (Wigmore and Molotch, 2023). We then calculated the first orthomosaic, we manually corrected motion blur in the corner areas, and produced the final orthomosaic, which was then calibrated using the ground-based Apogee temperature dataset (see the following section 2.3.7). The TIR orthomosaic has a reprojection error of 0.6 px and GCP errors in x, y and z-directions of 0.008 m, 0.003 m and 0.001 m. The workflow is summarized in Fig. 3.

2.3.7 TIR orthomosaic: Ground-based temperature calibration

To derive the surface temperature orthomosaic, we calibrated the brightness temperatures of the TIR orthomosaic using surface temperature data obtained from sea-ice-based observations. We calculated the snow surface temperature from the brightness temperature measured by the Apogee infrared radiometer, accounting for the contribution of the reflected fraction of downwelling longwave radiation measured with a Kipp and Zonen CGR4 pyrgeometer (Apogee Instruments INC., 2022):

https://doi.org/10.5194/egusphere-2025-1601
Preprint. Discussion started: 14 May 2025

$$T_{surface} = \sqrt[4]{\frac{T_{Apogee}^4 - (1-\epsilon)Lw_{\downarrow}/\sigma}{\epsilon}} \quad (4)$$

where $T_{surface}$ is the surface temperature (K), T_{Apogee} is the surface brightness temperature measured with the Apogee sensor (K), $\epsilon = 0.98$ is the snow thermal emissivity, and σ is the Stephan-Boltzman constant.

In Fig.6a, we present the surface temperature time series of the snow surfaces within the footprints of the two Apogee infrared radiometers during the flights, alongside the $T_{brightness}$ of the corresponding TIR images (with an RMSE of 0.58 ℃) that cover the two footprints. We extracted $T_{brightness}$ within the Apogee sensor footprints from the TIR images and plotted it against the Apogee-measured surface temperatures ($T_{surface}$) in Fig.6b. We calibrated the airborne brightness temperatures to surface temperatures by calculating the best (linear) fit between the Apogee-measured, sea ice-based surface temperatures $T_{surface}$ and the collocated, simultaneous TIR image brightness temperatures $T_{brightness}$. To match the airborne data points with the higher-resolution (10 s) sea ice-based measurements, we averaged the three $T_{surface}$ measurements taken before and after the $T_{brightness}$ timestamp. We used this dataset to calculate the linear fit:

$$T_{calibrated} = 0.68 * T_{brightness} - 4.44 \quad (5)$$

This equation is applied to each pixel in the TIR orthomosaic. The RMSE of the residuals of this linear fit is 0.48 ℃. The square root of the sum of the squared uncertainty of this fit, the square of the thermal camera uncertainty ($\pm$ 2 ℃), and the square of the RMSE associated with the NUC correction (0.58 ℃) provides a total uncertainty of $\pm$ 2.1 ℃ for the the surface temperature derived from airborne thermal imagery.

2.3.8 Detection of sediment deposition

In this study, we use the red band (wavelengths > 0.6 µm) of the RGB orthomosaic to detect visible sediment deposition on snow. Snow albedo is most sensitive to impurities in the visible wavelengths (Warren and Wiscombe, 1980), and we found the most contrast in the red band, where, qualitatively, sediment patches stand out more clearly against the bright snow background. We do not use the red band to quantify impurity levels because variations in camera settings during the flights affect the light captured, requiring standardization across the resultant images.

2.3.9 Irradiance calculation

We utilized the derived DEM to calculate the distribution of received solar radiation (irradiance) over the mapped surface roughness features, considering the surface aspect and slope and the solar position during the flight. Using a terrain-corrected radiative transfer model based on measured direct and diffuse components of shortwave radiation (Badosa et al., 2014), the model projects direct radiation onto an inclined surface using slope, aspect, solar zenith, and solar azimuth angles. Terrain shading is accounted for using the digital elevation model by Corripio (2003), and the measured diffuse radiation is applied to shaded areas. This approach follows established methods like those described by Dozier

https://doi.org/10.5194/egusphere-2025-1601
Preprint. Discussion started: 14 May 2025

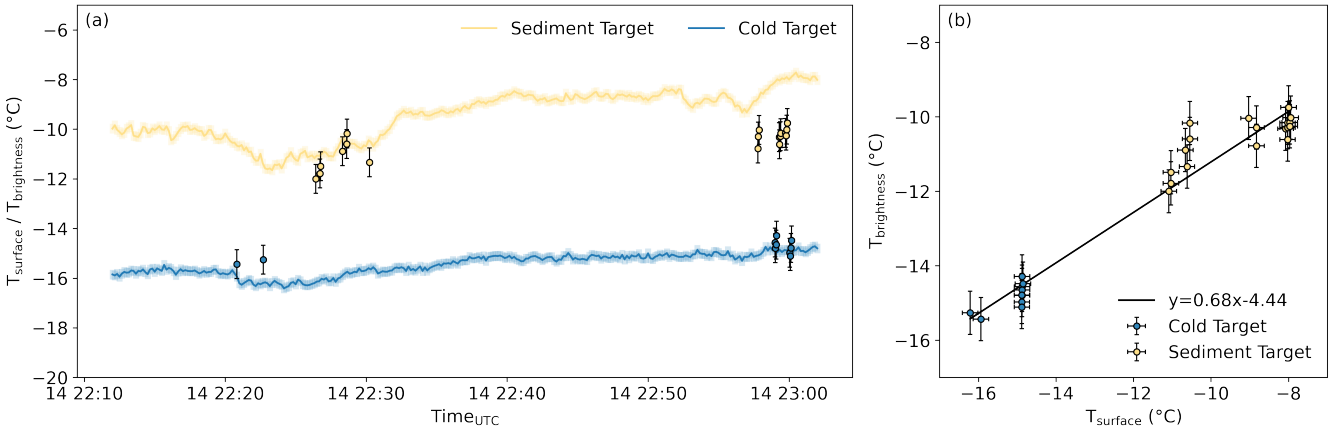

Figure 6. (a) The time series (line plots) of surface temperatures measured on November 14th, 2022 with the two Apogee sensors (Table 1) – snow with visible sediment particles (yellow), and clean snow without visible sediment particles (blue). The dots are $T_{brightness}$ from all TIR images (NUC corrected) that contain the Apogee sensor's footprint with the temperature anomaly RMSE of 0.58 °C that results from the correction equation (eq. 2 and 3). (b) Scatter plot with ground-based temperatures measured by Apogee sensors ($T_{surface}$) at the two targets against the $T_{brightness}$ from TIR images that encompass the footprints of these sensors. The black line is the best linear fit. The error bars indicate the temperature anomaly RMSE of 0.58 °C and the manufacturer's uncertainty for the Apogee sensor, respectively.

and Frew (1989). However, instead of calculating the radiative transfer through the atmosphere, we directly use the measured global and diffuse radiation during the flight window (594 Wm^{-2} and 71 Wm^{-2}, respectively), we calculated the angle between the sun's rays and the surface normal, considering the various slopes and aspects of the sea-ice surface features.

3 Results

Here, we present the results from our airborne and ground-based surveys over the 200x200 m field site of undeformed first-year landfast sea ice with relatively uniform snow cover. All airborne products have 9 cm/px resolution. Our UAV data include 1) an RGB orthomosaic, 2) a DEM, corrected with magnaprobe snow depth data used as a snow depth proxy, 3) a surface temperature orthomosaic, 4) red band intensity for the qualitative detection of surface dust and darker areas, and 5) modeled small-scale irradiance patterns, using the DEM to account for slope, aspect and shading. We analyze kernel density estimation (KDE) functions to identify patterns and correlations across sub-datasets (e.g. with and without visible sediment deposition). Our results reveal a complex system of snow-atmosphere interactions even within a snowpack initially defined as "flat" and relatively uniform.

The test field was situated on sea ice with an average thickness of 2.4 $\pm$ 0.04 m across 2449 measurements, showing relative variation of about 1 % (Fig. 7). Thickness ranged from 2.28 m to 2.52 m with a measurement uncertainty of 0.1 m

https://doi.org/10.5194/egusphere-2025-1601
Preprint. Discussion started: 14 May 2025

(Table 1). Since sea ice is buoyant, changes in thickness lead to only minor surface elevation variations, as most of the ice mass remains submerged. In contrast, snow depth varied significantly more at 32 % (see Table 2), even on this "flat" field, highlighting the snow cover's heterogeneity driven by wind processes.

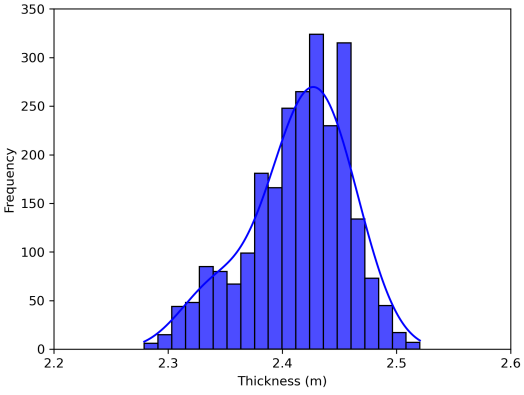

Figure 7. Sea ice thickness (m) distribution for 2449 measurements points surveyed with the EM31. The bandwidth parameter for the KDE function is 2.

Table 2. Mean thickness and Standard Deviation (STD) for the sea ice thickness (m), snow depth proxy (m) derived from the DEM and snow depth (m) measured with the magnaprobe, the number of data points (n) and the relative change (%) for each dataset.

Thickness	n	Mean ± STD (m)	Rel. Change (%)
Sea ice	2449	2.4 ± 0.04	1
Snow (DEM)	6211943	0.16 ± 0.06	30
Snow (magna)	813	0.1 ± 0.04	32

3.1 Airborne maps of snow depth proxy and surface temperature

We present the results of our airborne surveys in Fig. 8 and Fig. 9. The RGB orthomosaic in Fig. 8a provides an overview of the study area and allows us to identify areas with visible sediment deposition. The DEM (Fig. 8b) reveals relatively high variability in the snow depth proxy values, mainly due to wind-induced snow dunes (e.g. Fig. 8c, lower left). Although we expected dunes to align with the predominantly southerly winds during our campaign (Fig. A1b), we did not find a significant preference for the orientation of local aspects (Fig. 10c), which we assume is a proxy for dune orientation. While dune orientation is outside the scope of this study, evaluating a longer period of wind data preceding our field campaign would be necessary to understand dune alignment. The snow depth proxy ranges from 0 to 0.5 m, with a mean of 0.16 and a standard deviation (STD) of ± 0.06 m (Fig. 11a). We identified values exceeding 0.5 m as snow drifts around obstacles, such as measurement stations, solar panels, and flags.

In Fig. 9a, we present the TIR orthomosaic with temperatures ranging from -17.5 to -5 ℃. The mean temperature is -14.7 ± 0.4 ℃ (Fig. 11b). Temperatures exceeding -4 ℃ are caused by the measurement infrastructure and are masked in the TIR orthomosaic. Fig. 8c,d and Fig. 9c, d provide close-ups of an area that highlights variations in RGB color, DEM variations/snow depth, and surface temperatures. Areas with significant sediment deposition are visible by the eye as darker regions in the RGB orthomosaic (Fig. 8a, c) and red band orthomosaic (Fig. 9b, d). Those sediment patches are warmer than areas with cleaner snow as sediment has a lower albedo and absorbs more shortwave radiation (Fig. 9a, c). We also observe that the shaded sides of the snow dunes have lower temperatures (Fig. 9c, lower left) and are also darker in RGB and in the red band (Fig. 8c, Fig. 9d). In the RGB orthomosaic, two main features stand out: the

https://doi.org/10.5194/egusphere-2025-1601
Preprint. Discussion started: 14 May 2025

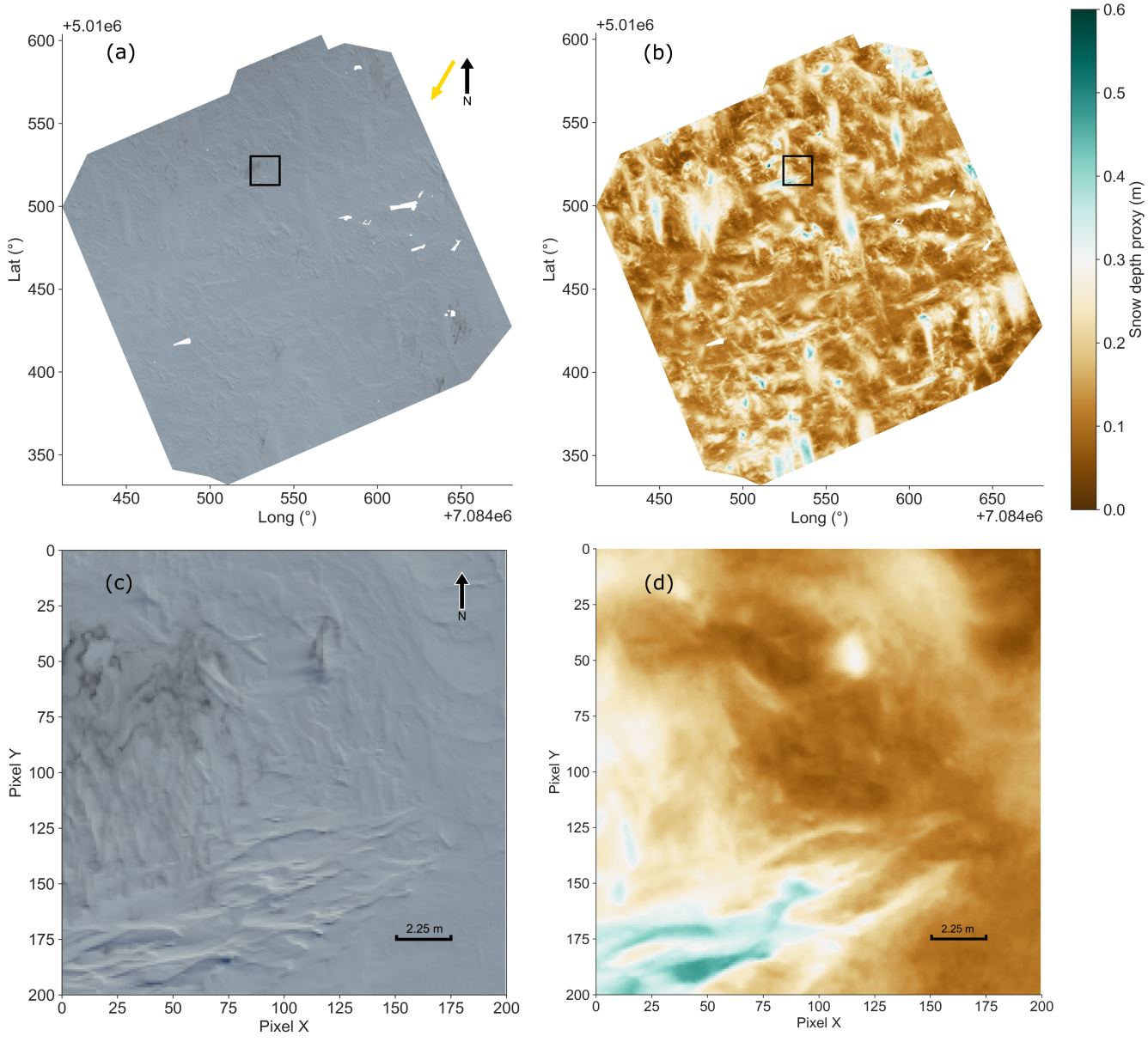

Figure 8. Airborne products (RGB orthomosaic and DEM) with 9 cm/px resolution. White spots are masked stations and targets (see Fig. A2). (a) RGB orthomosaic of the CS, with dark patches showing areas with sediment deposition. The yellow arrow indicates the sun's position in the north-east. (b) DEM of the CS showing the snow depth proxy (m). The color bar is set from 0 to 0.5 m to minimize the impact of remaining measurement stations and flags to better show the spatial variability of the snow cover. (c) Close-up of the RGB orthomosaic of an area with variations in snow topography and surface impurities. (d) Close-up of the snow depth proxy in the same area as (c).

https://doi.org/10.5194/egusphere-2025-1601
Preprint. Discussion started: 14 May 2025

sediment deposition in the northeastern corner of the image and the prominent snow dunes in the southern part. The snow dunes look "brighter", which could be due to snow thickness or due to irradiance (shading) effects. Both features, the sediment and the dunes, are visually distinguishable and provide additional information for understanding the drivers of surface temperature. Although the snowpack may appear relatively flat, there are significant variations in DEM height (snow depth, surface roughness, local slope/aspect), impurity content and surface temperatures.

3.2 Possible drivers of small-scale surface temperature variations: snow depth, sediment deposition or irradiance?

In this section, we use the UAV-derived maps of snow depth, surface temperature, and red bad values, as well as the derived map of solar irradiance, to try and disentangle the relevant drivers of local surface temperature variations. All statistical correlations are tabulated in Table A1.

3.2.1 Snow depth and surface temperature

To test our original hypothesis that snow surface temperatures are driven by snow depth (given relatively uniform sea ice thickness), we first explore the correlation between the snow depth proxy and snow surface temperature from our airborne maps (Fig. 8b and Fig. 9a). The scatter plot (Fig. 12a) reveals a very weak but statistically significant correlation (r_s=0.16, Table A1). Considering the very weak correlation, we can conclude that, for this particular case, our hypothesis that snow depth is the primary driver of surface temperature is not valid.

Given the visible sediment patches and their strong effect on albedo Warren and Wiscombe (1980), our next steps are to examine the correlation: a) in areas without visible sediment deposition and b) in areas dominated by visible sediment deposition (e.g. Fig. 8c, upper left area). To do this, we split the data into three sub-datasets: 1) the "entire field" dataset, containing 6,211,943 data points (approximately 99.9 % of the original dataset); 2) the "sediment" dataset, which includes 285,396 data points (approximately 5 %) from areas with visible sediment deposition and a small fraction of clean snow (Fig. A2b); and 3) the "no sediment" dataset, containing 341,473 data points (approximately 6 %) representing clean snow with no visible sediment (Fig. A2c). We delineated sediment patches by manually drawing polygonal areas around visible sediment deposits in QGIS (Fig. A2b). Each "sediment" patch also includes areas of clean snow. For the "no sediment" dataset, we randomly selected rectangular patches where no visible sediment was apparent, ensuring a similar number of samples for comparability. However, the "no sediment" dataset may still contain impurities that are not classified as sediment due to their subtle appearance in the RGB orthomosaic. Before manually delineating the patches, we tested various automatic R/G/B thresholds to identify impurities, but the results were unsatisfactory, partly because distinguishing between impurities and shaded areas proved challenging.

The "no sediment" dataset shows a similarly significant but very weak positive correlation between surface temperature and snow depth proxy(r_s=0.06, Fig.12g). This weaker correlation, compared to the "entire field" dataset, is likely due to a narrower temperature range caused by the absence of the warmer sediment patches. The "sediment" dataset shows a slightly stronger correlation (r_s=0.26, Fig.12d). It also has a higher mean surface temperature and greater temperature

https://doi.org/10.5194/egusphere-2025-1601
Preprint. Discussion started: 14 May 2025

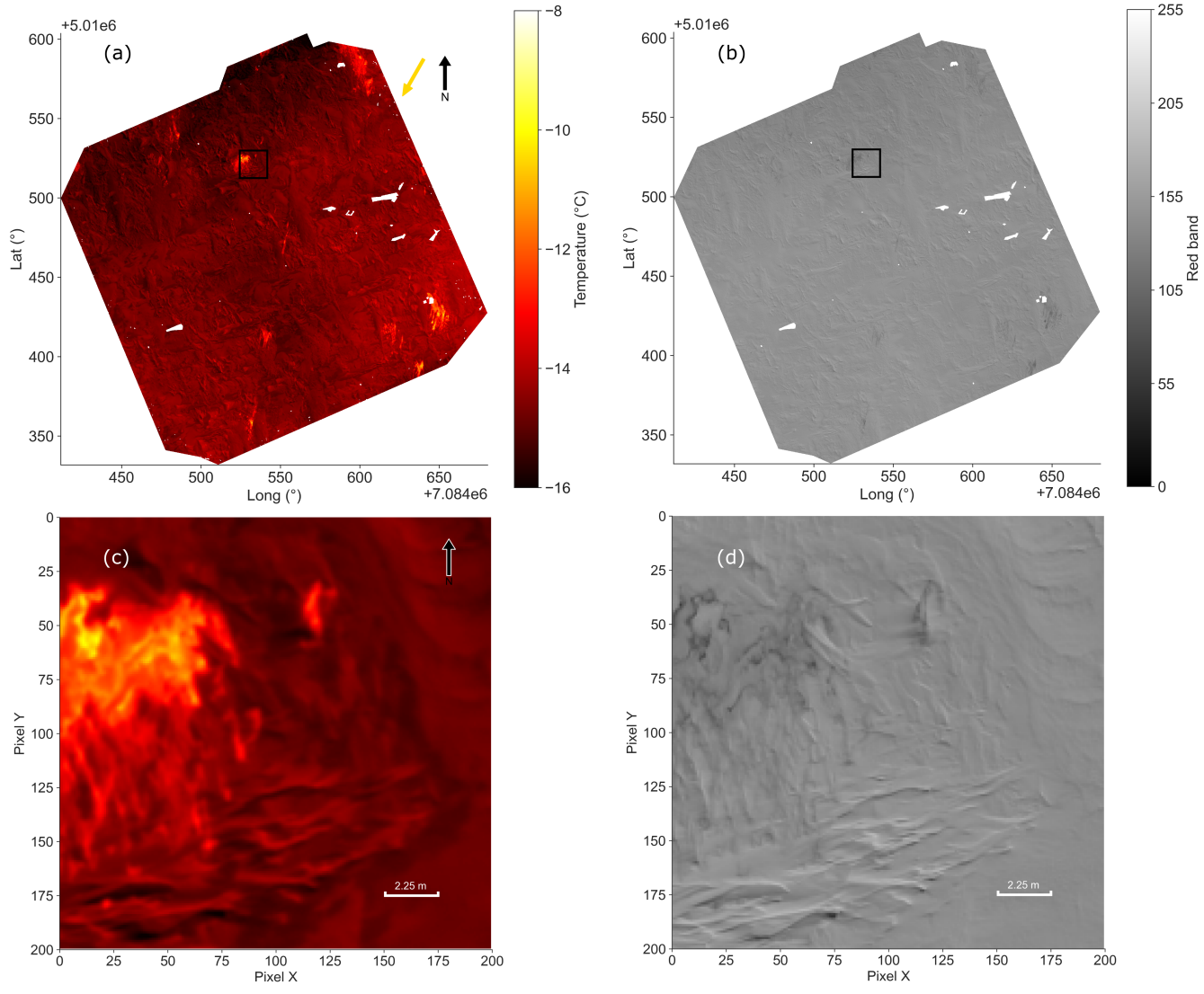

Figure 9. Airborne products (surface temperature and red band orthomosaics), both with 9 cm/px resolution. White spots are masked out stations and targets (see Fig. A2). (a) TIR orthomosaic of the CS with surface temperature in °C. The color bar is set from -8 to -16 °C to minimize the impact of remaining measurement stations, targets and flags and display the spatial variability of the snow surface temperature. (b) Red band (0 to 255) orthomosaic of the CS, with dark patches showing areas with sediment deposition. (c) Close-up of the same area with snow surface temperatures in °C. (d) Close-up of the same area with red band values.

https://doi.org/10.5194/egusphere-2025-1601
Preprint. Discussion started: 14 May 2025

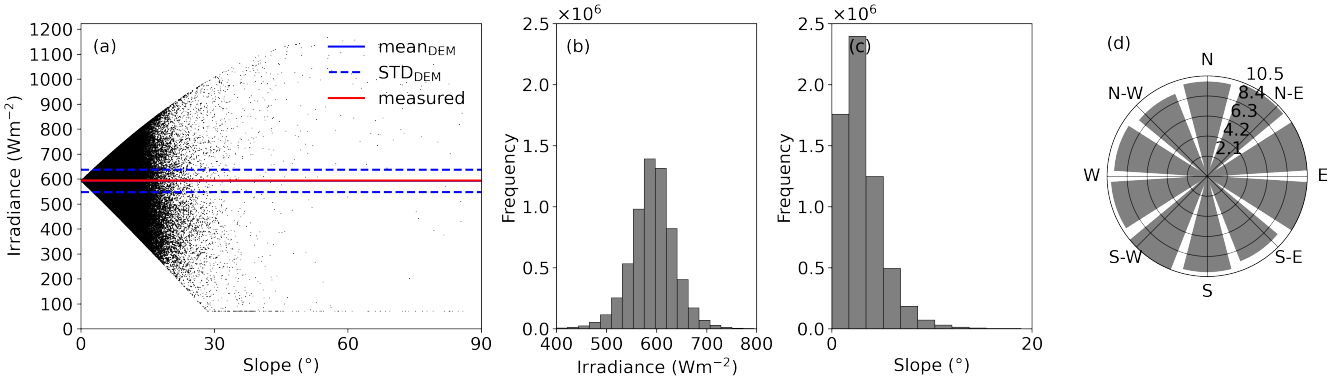

Figure 10. Scatter plot showing the relationship between slope and irradiance for the entire field, excluding stations and targets (a). (b) Histogram for the irradiance, the slope (c) and the aspect (d), each across the CS test field.

variability (-13.97 ± 0.82 ℃; Fig. 13b, Fig. 11f) compared to the "no sediment" dataset ((-14.8 ± 0.3 ℃); Fig. 13b, Fig. 11j). The larger variability in the "sediment" dataset suggests that the delineated sediment patches include both clean and "dirty" snow, likely reflecting variations in sediment concentration (Fig. 13b, Fig. 11f). The "sediment" dataset also shows a higher mean snow depth proxy and slightly greater variability (0.21 ± 0.07 m) compared to the "no-sediment" dataset (0.14 ± 0.05 m; Fig. 13a, Fig. 11e, i). In the "entire field" dataset, the mean snow surface temperature and snow depth proxy are -14.7 ± 0.4 ℃ and 0.16 ± 0.06 m, respectively (Fig. 13a,b; Fig. 11b, a). In summary, excluding visible sediment patches did not strengthen the validity of our hypothesis that snow depth is the primary driver of snow surface temperatures in the studied area.

3.2.2 Sediment deposition and surface temperature

Given the lack of a strong correlation between the snow depth proxy and snow surface temperature, we now investigate an alternative potential driver: surface impurities. Surface impurities largely influence the snow albedo and, consequently, surface temperatures (Warren and Wiscombe, 1980; Doherty et al., 2010; Réveillet et al., 2022). We use the red band of the orthomosaic as a proxy for "surface sediment darkness". While we acknowledge that the red band is not a perfect quantitative indicator for sediment concentration – and is also influenced by factors like shaded areas or variations in thin snow cover thickness – we must also consider the impact of the RGB camera's automatic settings (ISO, aperture, shutter speed). These settings likely adjusted in response to changing scene features and global and local illumination. Although we used the averaging blending mode to minimize exposure inconsistencies, this approach does not entirely eliminate the effect of varying camera responses across different flight lines. As a result, these camera-related factors may still contribute to the observed spread in the red band values and impact the strength of the observed correlations. However, we assume that in areas with high sediment concentrations, the impact of these factors on red band "brightness" is minimal. As in the previous section, we assess the correlation between surface temperature and red band values for

https://doi.org/10.5194/egusphere-2025-1601
Preprint. Discussion started: 14 May 2025

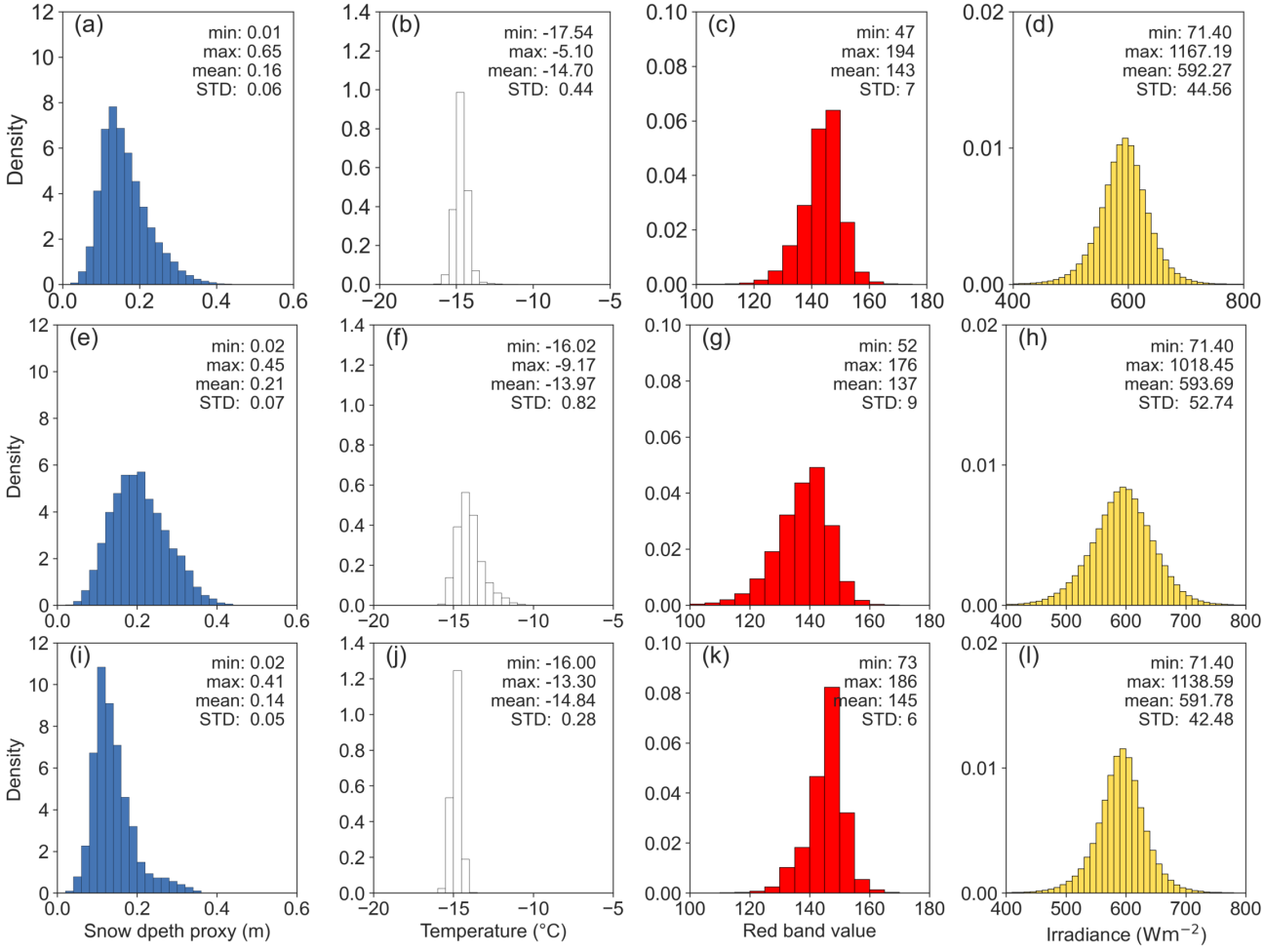

Figure 11. Histograms with PDFs for the snow depth proxy, surface temperature, red band values and irradiance for the three sub-datasets. The first row is the "entire field" dataset, the second row is the "sediment" dataset, and the last row is the "no sediment" dataset. The snow depth bin size (a,e and i) is 2 cm. The temperature bin size (b,f and j) is 0.5 °C. The red band bin size (c,g and k) is 5. The irradiance bin size (d, h, and l) is 10 Wm^{-2}.

the "entire field" dataset (Fig.12b), for the "sediment" dataset (Fig.12e) and for the "no sediment" dataset (Fig.12h). This approach helps us better understand the impact of visible sediment patches on the observed thermal signal.

While there is a weak but significant correlation between the surface temperature and red band intensity (r_s=0.35, Table A1) for the "entire field" dataset, the scatterplot (Fig.12b) shows an unexpected pattern. We explain this by looking at the "sediment" and "no-sediment" datasets separately. The "sediment" dataset shows a weak but significant negative correlation between the red band intensity and surface temperature (r_s=-0.23, Fig.12e). This means darker areas with

https://doi.org/10.5194/egusphere-2025-1601
Preprint. Discussion started: 14 May 2025

low red band intensity have higher surface temperatures, which aligns with expectations since sediment absorbs more shortwave radiation than snow (Ledley and Pfirman, 1997; Réveillet et al., 2022). The "no sediment" dataset shows a moderate positive correlation between red band intensity and surface temperature (r_s=0.4, Fig.12h), meaning darker areas are colder – the opposite of what we found in the "sediment" dataset. Considering that even clean snow likely contains small amounts of impurities, this result is initially surprising. However, a closer look suggests that the red band intensity variations in the "no sediment" dataset are likely due to differences in sunlight exposure, caused by small-scale topography like snow dunes (Fig. 8c,d, Fig. 9c,d). We now understand that the pattern in Fig. 12b reflects a combination of both datasets. The positive correlation for the "entire field" dataset is mainly driven by the "no sediment" (clean snow) areas, as the "sediment" dataset is around 20 times smaller and has little impact on the overall correlation statistics. The mean red band intensity is 137 ($\pm$ 9) for the "sediment" dataset and 145 ($\pm$ 6) for the "no sediment" dataset (Fig. 11g,k, Fig. 13c). The left-skew in red band values for all three areas suggests greater variability in the darker part of the red band orthomosaic. This happens because clean snow (most pixels) can't get much brighter in the red band. In contrast, variations in illumination and sediment concentration (fewer pixels) significantly affect the lower range of red band values.

In summary, we find that red band values correlate more strongly with surface temperature than the snow depth proxy across all three sub-datasets. This suggests that the red band intensity – influenced by 1) impurity concentration, 2) illumination variations, and 3) snow depth differences – predicts local surface temperatures. As shown in the previous subsection, snow depth variations are not the main driver of surface temperature. The stronger correlation between red band intensity and surface temperature in the "no sediment" dataset (r_s=0.4) compared to the "sediment" dataset (r_s=-0.23), leads us to hypothesize that local illumination conditions, shaped by variable surface topography may significantly impact local surface temperatures.

3.2.3 Local irradiance and surface temperature

Building on the previous section's findings that solar irradiance may significantly drive local temperature differences, we assess the correlation between modeled irradiance and surface temperatures across all three sub-datasets (Fig. 12c, f, i). Each sub-dataset shows a significant positive correlation between surface temperature and irradiance ("entire field": r_s=0.22, "sediment": r_s=0.22, "no-sediment": r_s=0.24). The mean irradiance is nearly identical for all three sub-datasets (Fig. 11d,h,l), but the variation (STD) is highest in the "sediment" dataset, likely due to higher snow depth and rougher surface (Fig. 11e).

Fig. 10a shows the spread of modeled irradiance against the local slope at each pixel. The cluster of data points with an irradiance of 71 Wm^{-2} present across the entire range of slope angles represents shaded areas receiving only diffuse shortwave radiation. The spatially averaged modeled irradiance for the test site, calculated using the measured snow topography (slope and aspect) to adjust the solar effective zenith angle, is 592 $\pm$ 45 Wm^{-2}, with values ranging from 71 to 1167 Wm^{-2}. This modeled mean aligns closely with the measured irradiance of 594 Wm^{-2} at the time of calculation, as we used observed shortwave radiation to determine atmospheric transmissivity and the fraction of the diffuse radiation. Over the entire flight period (about 40 minutes), the temporal mean measured irradiance was 593 $\pm$ 10 Wm^{-2}.

https://doi.org/10.5194/egusphere-2025-1601
Preprint. Discussion started: 14 May 2025

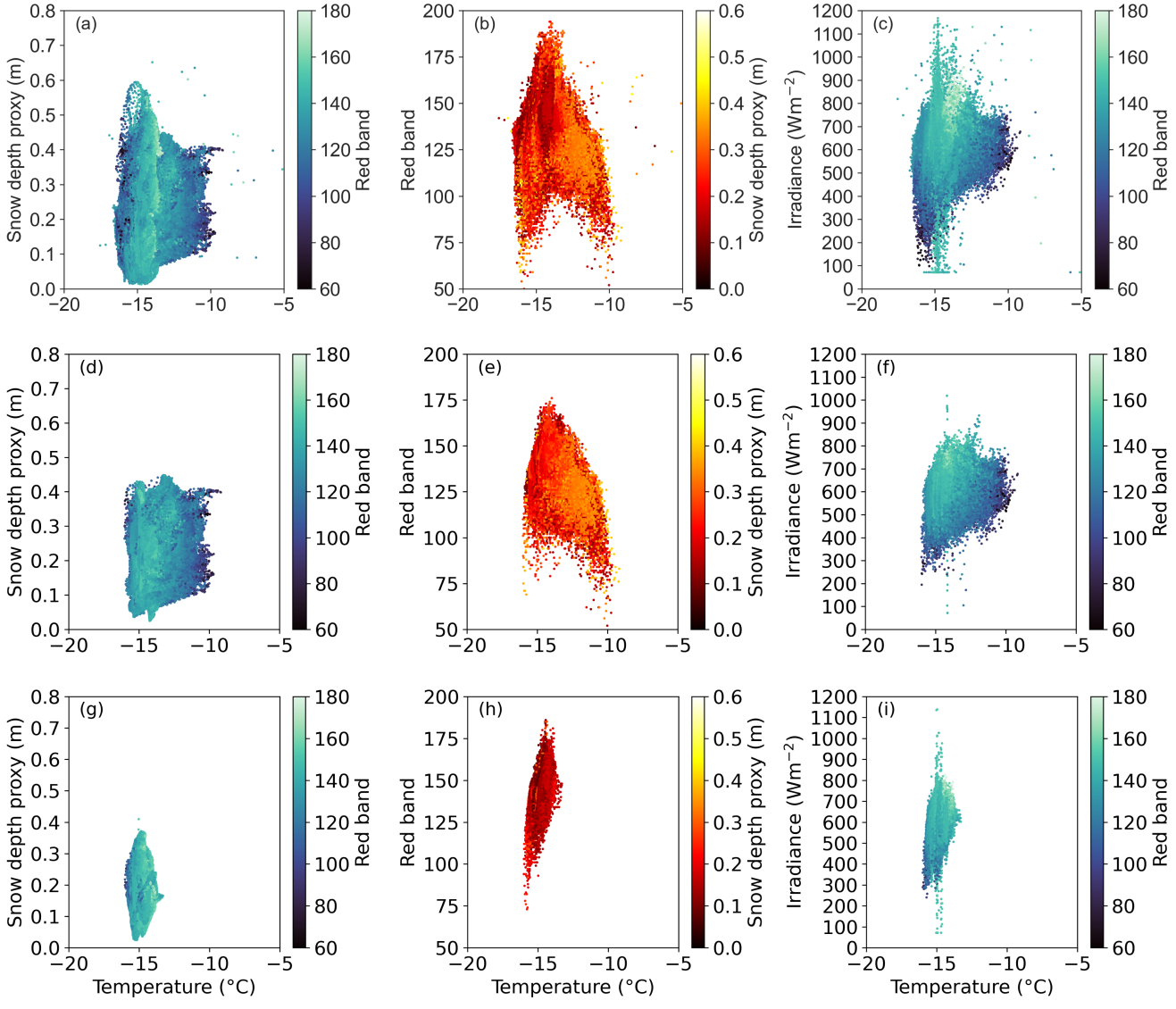

Figure 12. (a), (d) and (g) show the correlation between surface temperature and the snow depth proxy (the color bar is based on the red band values). (b), (e) and (h) show the surface temperature and irradiance (the color bar is based on the red band values). (c), (f) and (i) show the surface temperature and red band values (the color bar is based on the snow depth proxy). The first row contains data points for the "entire field", excluding targets and measurement stations. The second row (d, e, f) only contains data points within areas of visible sediment deposition ("sediment"). The last row displays data points for areas of clean snow without visible sediment deposition ("no sediment"), excluding targets and measurement stations. Details on correlation statistics are in Table A1.

https://doi.org/10.5194/egusphere-2025-1601
Preprint. Discussion started: 14 May 2025

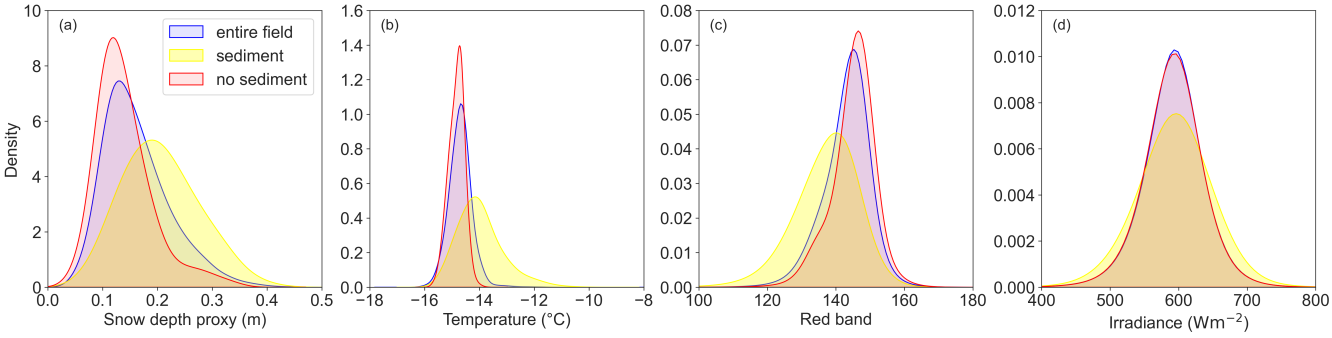

Figure 13. KDE plots for (a) the snow depth proxy, (b) the surface temperature, (c) the irradiance, and (d) red band values for the "entire field" (blue), the "sediment" dataset (yellow) and the "no sediment" dataset (red). The x-axis is cropped for a better display of the distribution, and the bandwidth parameter was set to 5.

The Gaussian distribution of slope and aspects in the DEM (Fig. 10c, d) suggests a near-random terrain pattern without a preferred alignment of the roughness features, which explains the normal distribution of the local irradiance calculation (Fig. 10b).

While the measured irradiance – representing irradiance on a flat plane – and the spatially average modeled irradiance (Fig. 10a, red and blue lines, respectively) are nearly identical because the overall energy reaching the area remains constant. However, if we account for the topography, the range (min-max) and variability (STD) in irradiance become significant. This highlights the strong influence of small-scale roughness on local irradiance.

4 Discussion

4.1 Technical considerations for high-resolution mapping of snow topography and snow surface temperature

Our study provides high-resolution airborne maps of a snow depth proxy and snow surface temperature over an area of up to 200 m. Producing accurate maps of these variables requires three key technical considerations:

1. **Precise georeferencing** is essential for reliable spatial accuracy, requiring high-accuracy GPS and a sufficient number of visible and thermal targets to co-locate RGB and thermal images. We recommend at least 10 GCPs for a study site of 200x200 m.

2. **Rigorous post-processing of TIR images** is critical to ensure accurate temperature data. We developed a correction algorithm that automatically detects and reduces temperature jumps caused by NUC correction events, minimizing sensor temperature drift and improving data accuracy. Our algorithm can be applied to various camera models, offering broad utility for studies beyond polar research.

https://doi.org/10.5194/egusphere-2025-1601
Preprint. Discussion started: 14 May 2025

3. **Ground-based temperature measurements** are necessary to validate airborne temperature surveys. Airborne temperature measurements should ideally be taken near local solar noon to capture peak solar radiation, minimize radiation variability, and maintain a high sun angle to reduce shading. Clear skies are preferable to avoid cloud shadows that alter the surface temperature, though consistent high cloud cover can also be acceptable. The "best" conditions depend on the specific purpose of the survey, but random intermittent cloud cover should always be avoided as it is problematic.

   At least two non-contact infrared radiometers (e.g. Apogee sensors or equivalent) should be set up during the flight to measure snow surface temperature and calibrate the airborne measurements. To ensure accurate calibration, there should be a significant temperature difference between targets (e.g. a hot target like sediment, sea ice or a temperature-controlled target with known emissivity, and a cold target like clean snow).

4. **Ground-based snow depth measurements** are necessary to validate and bias-correct airborne snow depth surveys (on flat sea ice) and calculate the snow depth proxy. These measurements should be taken in the flight area, though not necessarily during flight.

Additionally, a balance between area coverage and flight duration is necessary to avoid changes in local irradiance (e.g., the measured irradiance during the entire flight increased from 575 to 609 $\mathrm{W m^{-2}}$). The non-uniform snow cover and the potential imprecision of the magnaprobe GPS locations present a challenging validation setup. We used the magnaprobe measurements to correct the offset of the airborne DEM (Fig. 2). This approach is valid primarily due to the small range of variability in the sea ice thickness and the smooth sea ice surface. In areas with heterogeneous sea ice thickness and greater surface roughness – such as pack ice (Haas, 2004) or ridged ice (Itkin et al., 2023) – the DEM will reflect the combined topography of variable sea ice thickness, ridging, and snow depth.

4.2 The role of snow depth

We initially hypothesized that, assuming uniform sea ice thickness and smooth sea ice surface, thicker snow would result in lower surface temperatures due to its higher thermal insulation and albedo. However, our data show a weak positive correlation between the snow depth proxy and surface temperature, contradicting this hypothesis (Fig. 12a, Table A1). The presence of visible sediment depositions at the snow surface, which are associated with higher temperatures (Fig. 9c,d), prompted us to evaluate areas with and without sediment separately. We defined two sub-datasets for analyses: 1) the "sediment" dataset (areas with visible sediment, some clean snow), and 2) the "no sediment" dataset (areas with visible clean snow only). Both sub-datasets are of comparable size. The "no sediment" dataset shows no correlation between the snow depth proxy and surface temperature, further disproving our hypothesis that snow depth is the key driver of snow surface temperatures. In contrast, the "sediment" shows a weak but significant correlation between the snow depth proxy and surface temperature, suggesting that sediment deposition is influenced by the same wind processes as snow depth, with both snow and impurities accumulating in the same areas. This is supported by the higher mean snow depth in the "sediment" dataset (0.21 m) than in the "no sediment" dataset (0.14 m) (Fig. 11e, i). In summary, the positive correlation

https://doi.org/10.5194/egusphere-2025-1601
Preprint. Discussion started: 14 May 2025

that we observe between snow depth and snow surface temperatures is primarily driven by sediment deposition rather than snow depth itself. This emphasizes the role of sediment on albedo and radiation absorption rather than the role of snow depth on thermal resistance. This will have the effect that, when air temperatures rise later in the season, the increased solar radiation absorption by the sediment will reduce the snow specific surface area and accelerate snow melt, further decreasing the albedo and triggering the albedo feedback (Ledley and Pfirman, 1997; Skiles et al., 2018). While snow depth plays an important role in the energy balance of sea ice through albedo and thermal conductivity effects (Warren and Wiscombe, 1980), it is not the primary driver of surface temperatures in our case, even when excluding visible surface impurities.

4.3 The role of "darker areas": sediment or shadows?

Building on our finding that sediment strongly influences surface temperatures, we correlated the surface temperature with the red band values from the RGB orthomosaic. Sediment particles – like dust, soot, or organic matter – absorb more sunlight in the visible spectrum than clean snow (Tuzet et al., 2019; Cui et al., 2021). While the red band values do not directly affect the surface energy balance, we use them as a proxy for impurities.

The "sediment" dataset shows a weak negative correlation (r_s=-0.23) between red band values (where lower values represent "darker" pixels) and surface temperature – an expected result, because impurities generally increase radiation absorption. Surprisingly, the "no sediment" dataset showed a moderate positive correlation (r_s=0.4) between red band values and surface temperature, which was initially puzzling, because we saw no reason that darker red band values should have lower temperatures. We interpret this positive relationship through the influence of solar illumination and shading variations due to local topography: darker, shaded areas appear colder, while sunlit areas are warmer, leading to the observed correlation. In the "sediment" dataset, the red band values reflect a combination of sediment concentration (which drives a negative correlation with surface temperature) and local irradiance variations (which drive a positive correlation). This overlap results in a weak overall correlation (r_s=-0.23) in the "sediment" dataset. Despite the competing effects of impurities vs irradiance, the negative correlation is dominant, indicating that for areas with higher sediment concentrations, the effect of impurities on surface temperature outweighs that of local irradiance. The stronger correlation in the "no sediment" dataset (r_s=0.4) suggests that surface temperature in these areas is more directly driven by irradiance and shading than by the presence of impurities. Therefore, for clean snowpacks without significant sediment deposition, our results highlight the dominant role of solar illumination and shading in driving surface temperature and local energy balance.

Our discussion does not include the secondary effect of impurities, which leads to a lowering of albedo due to warmer snow temperatures and faster snow melt in the spring season. Furthermore, sediment deposition can also alter the surface texture and roughness of the snow through preferential melt. A rougher snow surface traps the light reflected multiple times between protruding features and lowers the effective solar zenith angle, leading to reduced reflectance (Manninen et al., 2021).

https://doi.org/10.5194/egusphere-2025-1601
Preprint. Discussion started: 14 May 2025

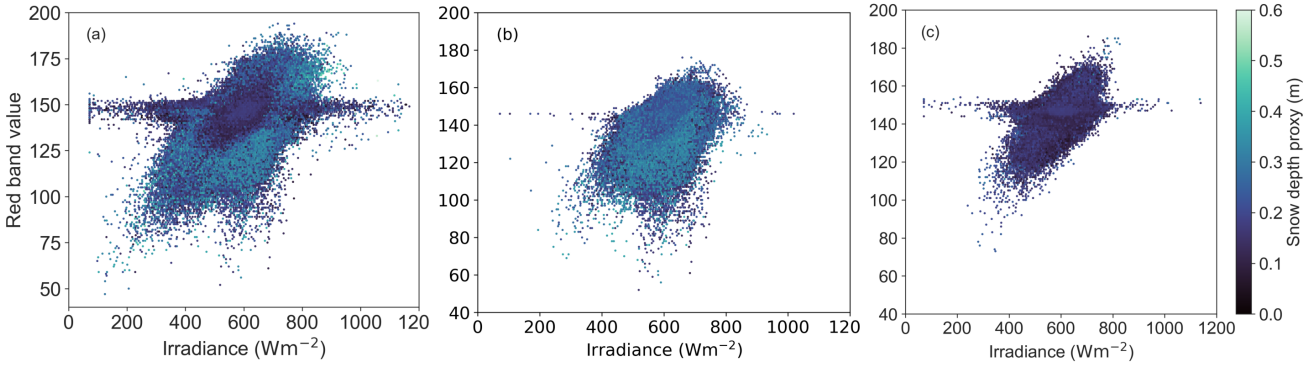

Figure 14. Correlation between irradiance (Wm^{-2}) against red band intensity for "entire field" dataset (r_s=0.44) (a), "sediment" dataset (r_s=0.41) (b) and "no sediment" dataset (r_s=0.44) (c). We cannot with certainty explain the horizontal cluster from about 140 to 160 red band intensity that stretches across a larger range of irradiances than the rest of the data. However, the only connection we found for this cluster is snow depth or the associated surface roughness, because the cluster disappears for higher snow depths, as discussed in A5 (Fig. A3). This cluster, however, has a low data density (Fig. A3d) and is therefore outside of the scope of our study.

4.4 The role of irradiance

We just proposed that the red band values are likely connected to local irradiance, which is why our results show a correlation between red band intensity and surface temperatures. To test this hypothesis that the red band intensity is connected to irradiance (illumination and shading), we calculated topography-dependent irradiance for each pixel. We found a moderate correlation between the red band values and irradiance across all three datasets (Table A1), confirming that red band value variations are at least partially caused by irradiance variations (Fig. 14).

In the "no sediment" dataset, the correlation between red band values and irradiance (r_s=0.44) is comparable to the correlation between red band values and surface temperature (r_s=0.4), supporting our hypothesis that irradiance is a key driver of surface temperature. While the the correlation between red band values and irradiance for the "sediment" dataset is the same (Fig. 13d) because the irradiance depends on topography only, the values associated with sediment deposition exert a more dominant influence on surface temperature (Fig. 12e), suggesting that sediment has a stronger impact on surface heating than shading and irradiance have on surface cooling.

Even at our relatively flat site, the topography-dependent irradiance shows considerable variations (Fig. 10) with 95% of the data (2 STD) ranging between 502-682 Wm^{-2} – approximately $\pm$ 20% from the areal mean. This spatial variability in irradiance (and surface temperature) arises from high surface roughness and the influence of seemingly small changes in local topography on the surface temperature, primarily by altering the apparent solar zenith angle(Wiscombe and Warren, 1980). While these small-scale topographic variations do not affect mean areal irradiance – since they cannot change the total incoming radiation over a given area – they may nonlinearly influence the local snowpack energy balance (Weller, 1969; Hao et al., 2022). This can lead to localized temperature gradients (vertical and horizontal) and associated

https://doi.org/10.5194/egusphere-2025-1601
Preprint. Discussion started: 14 May 2025

changes in snow microstructure. For example, temperature differences between sun-exposed and shaded sides of dunes can drive lateral heat movement(Sturm and Holmgren, 1994), altering the snow microstructure and impacting both albedo and thermal conductivity(Clemens-Sewall et al., 2024). In more extreme cases, this lateral heat transfer and associated metamorphism can result in changes to snow height and surface topography through snow sublimation (Gow, 1965; Orheim, 1968; Weller, 1969). Later in the season, when surface temperatures approach 0 ℃, even small variations in local irradiance can trigger differential melting, freezing and densification processes, further amplifying spatial variability in the snowpack.

Moreover, surface roughness – even from smaller slopes – can distort the spectral shape of albedo through multiple reflections, leading to inaccurate estimates of solar radiation interception (Picard et al., 2020; Manninen et al., 2021). Slopes as small as 1 ° can cause these distortions, with their complexity increasing with increasing slopes. Accurate estimates of albedo, therefore, require accounting for surrounding terrain at the full range of scales(Picard et al., 2020; Manninen et al., 2021; Larue et al., 2020).

We demonstrate that if models do not account for snow surface roughness – either due to the lack of availability of local topography data or insufficient model resolution – they tend to underestimate the variability in irradiance and simplify the amount of energy available for localized snow metamorphism and melt processes, particularly in areas with pronounced topography variations. Our results suggest that incorporating more detailed representations of snow surface topography (or a scale-appropriate parameterization, such as a statistical distribution of topographical parameters) and its influence on irradiance could improve the accuracy of energy balance models for sea ice and snow-covered regions. Further studies are needed to quantify the impact of surface roughness on surface energy balance and refine models to better capture these variations under diverse environmental conditions. Future efforts should focus on evaluating the sensitivity of large-scale models to the spatial variability of snow and enhancing their ability to represent surface roughness effects on irradiance, ultimately leading to more accurate predictions of sea ice melt dynamics.

4.5 Limitations and future directions

While this study contributes valuable insights, we acknowledge several limitations and also outline directions for future research. The spatial scale of our study is constrained by flight duration, which is limited by battery life. To minimize temperature fluctuations caused by changing solar radiation and fluctuating cloud coverage, which drive changes in surface temperature, we restricted flight time. For our 200x200 m test site, we used two pairs of batteries and completed the survey in two 20-minute flights. During this time, solar radiation gradually increased from 575 $\mathrm{Wm^{-2}}$ to 609 $\mathrm{Wm^{-2}}$, and our TIR surface temperature map was generated using data from both flights, which were conducted close to solar noon to mitigate radiation changes.

Our findings show that irradiance and impurities are the strongest predictors of surface temperatures for this test site and play a key role in the energy balance. However, our method for calculating the snow depth proxy is limited to flat and smooth sea ice. Surface elevation cannot reliably serve as a proxy for high-resolution snow depth on deformed or uneven sea ice, which exhibits significant spatial heterogeneity in thickness and surface roughness. Consequently,

https://doi.org/10.5194/egusphere-2025-1601
Preprint. Discussion started: 14 May 2025

surface topography on deformed or rough sea ice cannot reliably serve as a proxy for snow depth. The role of irradiance, however, is even more significant in regions with greater surface roughness.

Looking ahead, we plan to expand the applicability of the methods introduced in this study by testing them at other sites with different snow and sea ice conditions. Applying these techniques to areas with deformed sea ice and ridges (surface temperature and roughness only), or borderline zones with bare ice and thin snow patches will provide valuable insights into surface drivers of the sea ice energy balance. This will also refine the robustness and adaptability of our methods. By validating them across diverse test sites, we aim to enhance the utility for broader applications. Ultimately, we aim for using such high-resolution data to help improve parameterizations in climate models, as well as provide data for satellite remote sensing algorithms in more heterogeneous environments.

5 Summary and Conclusions

This study demonstrates that UAV-based remote sensing is an effective method for assessing snow depth and surface temperatures on uniform (flat and smooth) landfast sea ice in the Ross Sea, Antarctica. By utilizing high-resolution RGB and TIR orthomosaics alongside a DEM, we successfully mapped the snow depth, surface temperature, and visible sediment deposition. The DJI Matrice 30T UAV, combined with precise ground georeferencing and the novel NUC correction algorithm introduced in this study, provides viable insights and solutions for the challenges of measuring airborne surface temperatures. The technical contribution here lies in addressing and mitigating several key sources of error that can impact airborne temperature measurements. Our algorithm for correcting NUC camera calibration events has broader applicability, extending beyond polar research and offering valuable tools for many users. These solutions, though innovative, require a reasonably high ground-truthing effort, which may not be feasible in less extensive campaigns. However, they highlight the complexity of achieving accurate surface temperature measurements in such an environment. Our work underscores the feasibility and importance of conducting high-resolution snow measurements on landfast sea ice. While our methods of retrieving surface roughness and temperature are valid for all ice types, we acknowledge that using the DEM as a snow depth proxy in heterogeneous ice environments is not valid.

Our UAV mapping of high-resolution surface topography of snow and ice surface temperatures (Fig. 8, 9) emphasizes the spatial variability of snow and its relatively large surface roughness, as well as the impact of even small changes in local topography on surface temperatures. By quantifying small-scale spatial variability, we provide insights into how these variations may influence the surface energy balance. These findings also shed light on the complexities of modeling snow and ice in sea ice environments.

The statistical analysis of the high-resolution data highlights the impact of small-scale snow surface topography, which drives irradiance variability and influences the evolution of snow-covered sea ice. We discovered that, in our case study, assuming a flat ice surface without surface roughness significantly underestimated modeled irradiance variability ($592 \pm 45\,\mathrm{W m^{-2}}$ ranging from 71 to $1167\,\mathrm{W m^{-2}}$). This is relevant because the relationship between irradiance and temperature can exhibit non-linearities; for instance, changes in slope or aspect can disproportionately affect the amount of solar

https://doi.org/10.5194/egusphere-2025-1601
Preprint. Discussion started: 14 May 2025

radiation received, leading to localized heating effects. This non-linearity can enhance the thermodynamic response of snow-covered surfaces, influencing not only the melt rates but also sediment transport processes, as areas receiving more concentrated irradiance may experience accelerated melting compared to their surroundings.

Future research should focus on investigating model sensitivity to local irradiance values at different scales and refining predictive models to better forecast changes in polar energy budgets. The findings and methods from our study provide valuable insights for both polar research and broader scientific applications, underscoring the need for higher resolution data to improve our understanding energy balance drivers across scales in these critical environments.

Appendix A: Additional figures and statistics

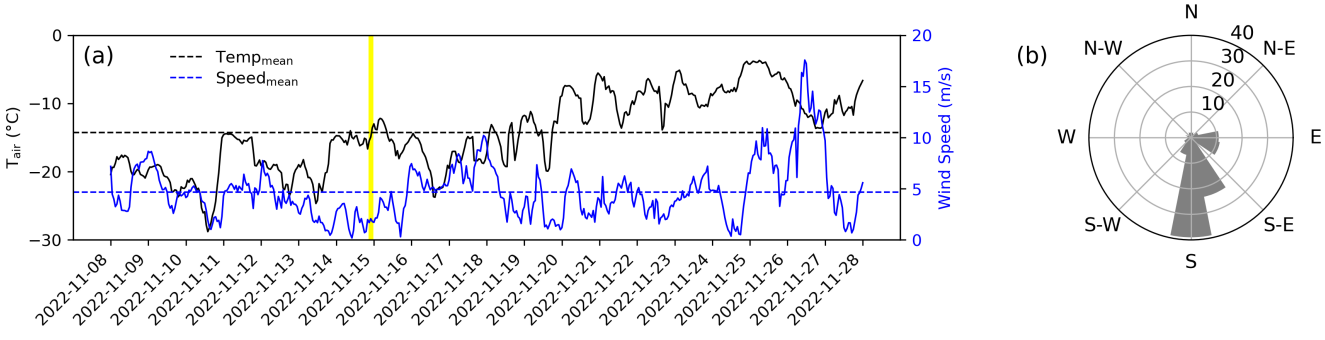

Figure A1. (a) Hourly air temperature and wind speed average during field campaign at CS test field. The vertical yellow bar indicates the UAV mission. (b) The prevailing wind directions at the CS test field during the field campaign.

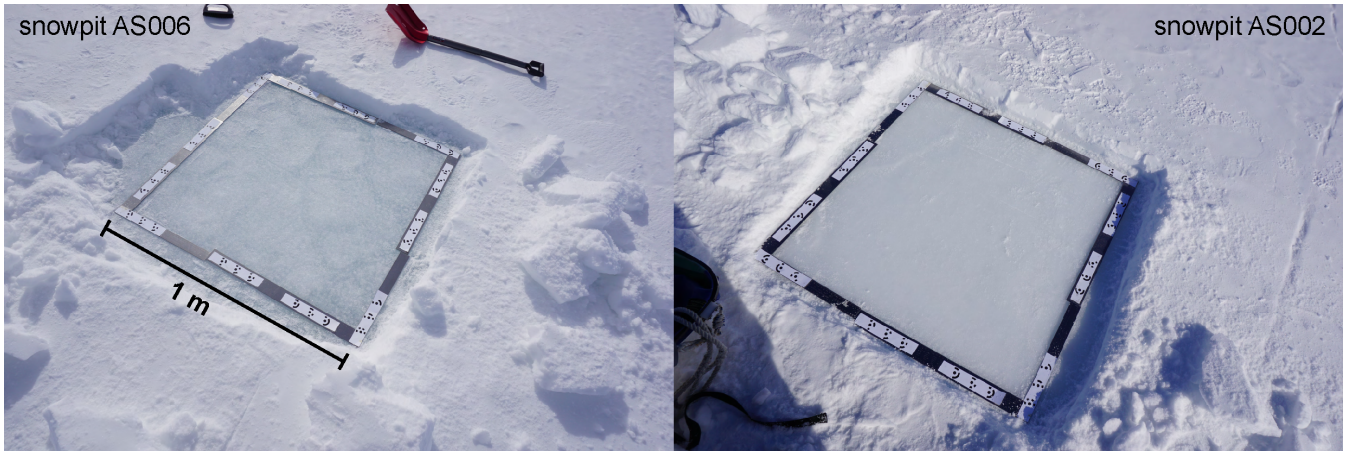

Figure A1. Sea ice surface at two different snowpit locations (AS006, AS002) inside the 200x200 m CS test field during our field campaign showing the flat and smooth sea ice surface.

https://doi.org/10.5194/egusphere-2025-1601
Preprint. Discussion started: 14 May 2025

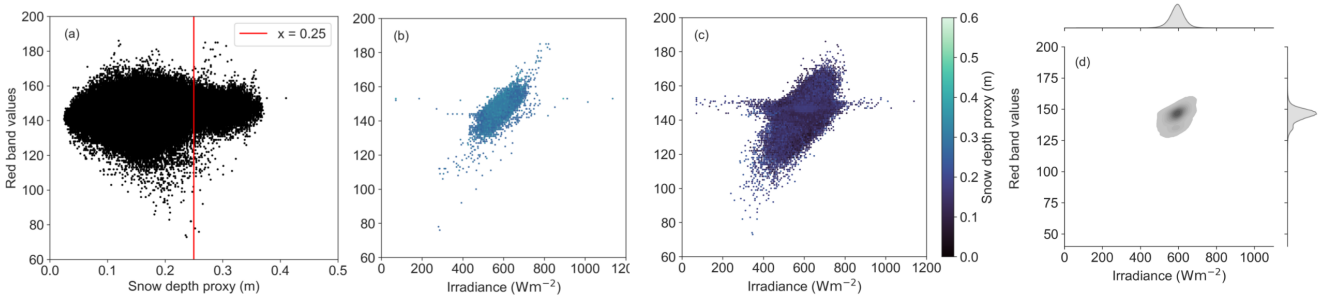

Figure A3. (a) scatter plot of red band intensity versus snow depth proxy (m) for "no sediment" sub-dataset (r_s=0.08). The red line indicates the visible cluster separation. (b) Scatter plot of red band intensity versus irradiance (Wm^{-2}) for "no sediment" dataset, considering only data points where the snow depth proxy exceeds 0.25 m (r_s=0.69). (c) Same as (b) but for snow depth proxy values below 0.25 m (r_s=0.41). Statistics details are provided in TableA1. These plots reveal that the horizontal cluster observed the red band intensity range of 140 to 160 disappears when considering only snow depth proxy values is connected to the snow depth as it disappears when considering only snow depth proxy values above 0.25 m, indicating a connection to snow depth. For snow depth proxy values below 0.25 m, the entire irradiance range is present, suggesting a link to surface roughness. However, the red band intensity shows no direct dependence on the surface roughness, and a more detailed analysis is beyond the scope of this study. (d) Highlights that the horizontal extent of the cluster corresponds to a region with low data density.

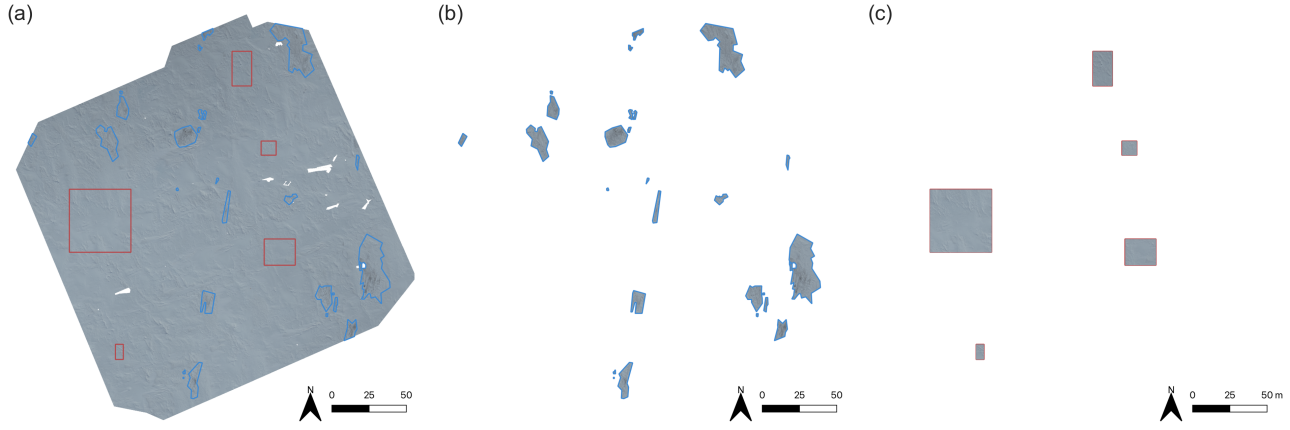

Figure A2. Masks used to create the three sub-data sets "entire field" (a), "sediment" (b) and "no sediment" (c) in the RGB orthomosaic.

Data availability. Raw data is available at: (Dadic et al., 2025). Processed data is available at: (Martin et al., 2025).

https://doi.org/10.5194/egusphere-2025-1601
Preprint. Discussion started: 14 May 2025

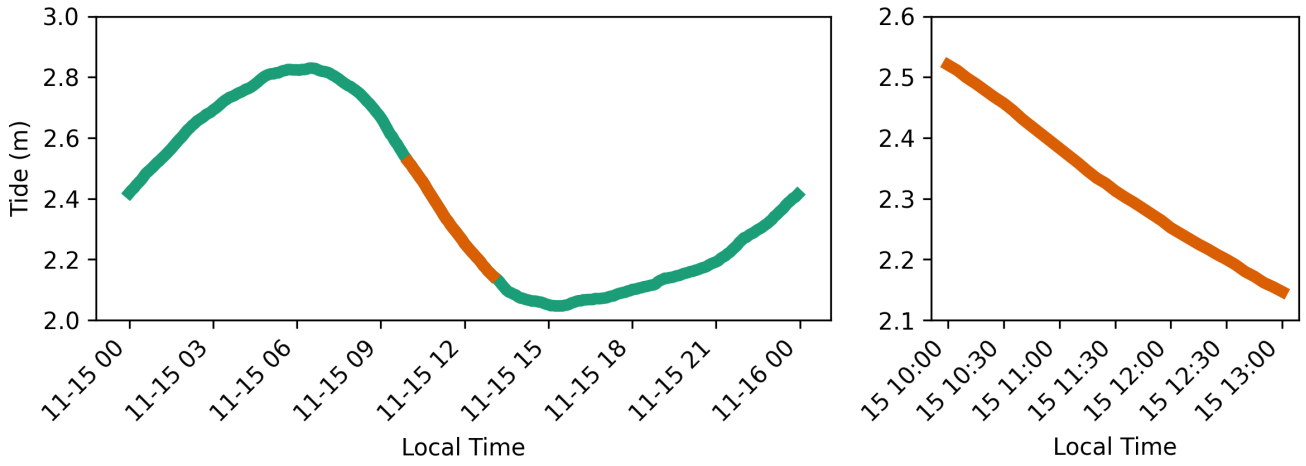

Figure A4. Tidal movements (m) at the Scott Base tidal gauge from the sea level recorder (nitrogen bubbler system with a paroscientific pressure transducer located on a bottom-mounted spigot of the osmosis boom and barometer). The data is recorded in 5 minute intervals.

Table A1. Statistics table for Fig. 10. Entire field: all data points excluding targets and measurement stations. Sediment: data points within areas of visible sediment deposition (and clean snow), excluding targets and measurement stations in these areas. No sediment: areas with no visible sediment deposition, excluding targets and measurement stations. The three datasets are displayed in Fig. A2. The correlation strengths are formatted as plain (very weak), *italic* (weak), **bold** (moderate), and underlined (strong) font styles.

Parameter A	Parameter B	Data points	Spearman (r_s)	p-value (α = 0.01)	Info
Temperature	*Snow depth proxy*	*6211943*	*0.16*	*<1e-16*	*entire field*
Temperature	**Snow depth proxy**	**285396**	**0.26**	**<1e-16**	**sediment**
Temperature	Snow depth proxy	341473	0.06	<1e-16	no sediment
Temperature	**Red Band**	**6211943**	**0.35**	**<1e-16**	**entire field**
Temperature	*Red Band*	*285396*	*-0.23*	*<1e-16*	*sediment*
Temperature	**Red Band**	**341473**	**0.40**	**<1e-16**	**no sediment**
Temperature	*Irradiance*	*6211943*	*0.22*	*<1e-16*	*entire field*
Temperature	*Irradiance*	*285396*	*0.22*	*<1e-16*	*sediment*
Temperature	*Irradiance*	*341473*	*0.24*	*<1e-16*	*no sediment*
Red band	**Irradiance**	**6211943**	**0.44**	**<1e-16**	**entire field**
Red band	**Irradiance**	**285396**	**0.41**	**<1e-16**	**sediment**
Red band	**Irradiance**	**341473**	**0.44**	**<1e-16**	**no sediment**
Red band	Snow depth proxy	341473	0.08	<1e-16	no sediment
Red band	Snow depth proxy (>0.25 m)	16965	0.69	<1e-16	no sediment
Red band	**Snow depth proxy (<0.25 m)**	**324508**	**0.41**	**<1e-16**	**no sediment**

https://doi.org/10.5194/egusphere-2025-1601
Preprint. Discussion started: 14 May 2025

Author contributions. JM, RD, BA, RP, OW: Methodology development, measurement campaign conceptualization. JM, RD, RP: Data acquisition. JM: Data processing, analysis, visualization, writing (original draft, review, editing). RD: Project administration, funding acquisition, conceptualization, data processing, analysis, writing (review, editing). BA: Project administration, funding acquisition, data processing, analysis, visualization, writing (review, editing). RP: Analysis, conceptualization, writing (review, editing). OW: Data processing, conceptualization, analysis, writing (review, editing). LV: Data processing, writing (review, editing).

Competing interests. The authors declare that they have no conflict of interest.

Acknowledgements. Data sets used in this manuscript were produced as part of the Marsden Fund **Grant/Award: 21-VUW-103**, the **EU H2020 PolarRES project** (grant no. 101003590) and by the Research Council of Finland through the **IceScales project** (contract 364939). We thank all people involved in organizing the 2022 expedition to McMurdo Sound Antarctica, especially Wolfgang Rack (University of Canterbury), Huw Horgan (Antarctic Research Centre), Greg Leonard (University of Otago), Inga Smith (University of Otago), Martin Schneebeli and Matthias Jaggi (WSL Institute for Snow and Avalanche Research), Nathalie Robinson (Antarctic Research Centre, NIWA), Dao Polsiri (Antarctic Research Centre) and Darcy Mandeno (Antarctic Research Centre). We acknowledge the international logistics support by the WSL Centre for Snow and Avalanche Research SLF (Switzerland), the Finnish Meteorological Institute FMI (Finland), the Antarctic Research Centre (New Zealand) and Antarctica New Zealand, including the Scott Base 2022/2023 staff.

https://doi.org/10.5194/egusphere-2025-1601
Preprint. Discussion started: 14 May 2025

References

Apogee Instruments INC.: Apogee SI-100 User Manual, Tech. rep., Apogee Instruments, https://www.apogeeinstruments.com/content/SI-100-manual.pdf, 2022.

Arndt, S. and Paul, S.: Variability of winter snow properties on different spatial scales in the Weddell Sea, Journal of Geophysical Research: Oceans, 123, 8862–8876, https://doi.org/10.1029/2018JC014447, 2018.

Arndt, S., Meiners, K. M., Ricker, R., Krumpen, T., Katlein, C., and Nicolaus, M.: Influence of snow depth and surface flooding on light transmission through Antarctic pack ice, Journal of Geophysical Research: Oceans, 122, 2108–2119, https://doi.org/10.1002/2016JC012325, 2017.

Badosa, J., Wood, J., Blanc, P., Long, C. N., Vuilleumier, L., Demengel, D., and Haeffelin, M.: Solar irradiances measured using SPN1 radiometers: Uncertainties and clues for development, Atmospheric Measurement Techniques, 7, https://doi.org/10.5194/amt-7-4267-2014, 2014.

Bradski, G.: The OpenCV Library, Dr. Dobb's Journal of Software Tools, 25, 122–125, https://doi.org/https://www.drdobbs.com/open-source/the-opencv-library/184404319#, 2000.

Brandt, R. E., Warren, S. G., Worby, A. P., and Grenfell, T. C.: Surface albedo of the Antarctic sea ice zone, Journal of Climate, 18, 3606 –3622, https://doi.org/10.1175/JCLI3489.1, 2005.

Brandt, R. E., Warren, S. G., and Clarke, A. D.: A controlled snowmaking experiment testing the relation between black carbon content and reduction of snow albedo, Journal of Geophysical Research: Atmospheres, 116, https://doi.org/10.1029/2010JD015330, 2011.

Brett, G. M., Irvin, A., Rack, W., Haas, C., Langhorne, P. J., and Leonard, G. H.: Variability in the distribution of fast ice and the sub-ice platelet layer Near McMurdo ice shelf, Journal of Geophysical Research: Oceans, 125, e2019JC015678, https://doi.org/10.1029/2019JC015678, 2020.

Buhler, Y., Adams, M. S., Bosch, R., and Stoffel, A.: Mapping snow depth in alpine terrain with unmanned aerial systems (UASs): Potential and limitations, Cryosphere, 10, 1075–1088, https://doi.org/10.5194/tc-10-1075-2016, 2016.

Callaghan, T. V., Johansson, M., Brown, R. D., Groisman, P. Y., Labba, N., Radionov, V., Barry, R. G., Bulygina, O. N., Essery, R. L., Frolov, D. M., Golubev, V. N., Grenfell, T. C., Petrushina, M. N., Razuvaev, V. N., Robinson, D. A., Romanov, P., Shindell, D., Shmakin, A. B., Sokratov, S. A., Warren, S., and Yang, D.: The changing face of arctic snow cover: A synthesis of observed and projected changes, Ambio, 40, 17–31, https://doi.org/10.1007/s13280-011-0212-y, 2011.

Clemens-Sewall, D., Polashenski, C., Perovich, D., and Webster, M. A.: The importance of sub-meter-scale snow roughness on conductive heat flux of Arctic sea ice, Journal of Glaciology, pp. 1–6, https://doi.org/10.1017/jog.2023.105, 2024.

Corripio, J. G.: Vectorial algebra algorithms for calculating terrain parameters from dems and solar radiation modelling in mountainous terrain, International Journal of Geographical Information Science, 17, 1–23, https://doi.org/10.1080/713811744, 2003.

Cui, J., Shi, T., Zhou, Y., Wu, D., Wang, X., and Pu, W.: Satellite-based radiative forcing by light-absorbing particles in snow across the Northern Hemisphere, Atmospheric Chemistry and Physics, 21, 269–288, https://doi.org/10.5194/acp-21-269-2021, 2021.

Da Jiang Innvoations (DJI): DJI Matrice 30T Manual, Tech. rep., DJI, https://www.dji.com/matrice-30/downloads, 2022.

Dadic, R., Martin, J., Pirazzini, R., Anderson, B., Cheng, B., Wigmore, O., Jaggi, M., Schneebeli, M., Leonard, G., Smith, I., Horgan, H., Martin, A., Dean, S., Blixt, I., Thompson, J., Leemann, M., Harbeke, F., Rack, W., Vargo, L., Feng, X., Wolfsperger, F., and Robinson, N.: Snow on Antarctic Sea Ice - McMurdo Sound 2022, https://doi.org/10.16904/envidat.633, 2025.

https://doi.org/10.5194/egusphere-2025-1601
Preprint. Discussion started: 14 May 2025

Doherty, S. J., Warren, S. G., Grenfell, T. C., Clarke, A. D., and Brandt, R. E.: Light-absorbing impurities in Arctic snow, Atmospheric Chemistry and Physics, 10, 11 647–11 680, https://doi.org/10.5194/acp-10-11647-2010, 2010.

Dozier, J. and Frew, J.: Rapid calculation of terrain parameters for radiation modeling from digital elevation data, in: Digest - International Geoscience and Remote Sensing Symposium (IGARSS), vol. 3, pp. 963–969, https://doi.org/10.1109/igarss.1989.576516, 1989.

Eicken, H., Lange, M. A., and Wadhams, P.: Characteristics and distribution patterns of snow and meteoric ice in the Weddell Sea and their contribution to the mass balance of sea ice, Annales Geophysicae, 12, 80–93, https://doi.org/10.1007/s005850050038, 1994.

Estey, L. H. and Meertens, C. M.: TEQC: The multi-purpose toolkit for GPS/GLONASS data, GPS Solutions, 3, 42–49, https://doi.org/10.1007/PL00012778, 1999.

Gaffey, C. and Bhardwaj, A.: Applications of unmanned aerial vehicles in cryosphere: Latest advances and prospects, Remote Sensing, 12, 948, https://doi.org/10.3390/rs12060948, 2020.

Gough, A. J., Mahoney, A. R., Langhorne, P. J., Williams, M. J., Robinson, N. J., and Haskell, T. G.: Signatures of supercooling: McMurdo Sound platelet ice, Journal of Glaciology, 58, 38–50, https://doi.org/10.3189/2012JoG10J218, 2012.

Gow, A. J.: On the Accumulation and Seasonal Stratification Of Snow at the South Pole, Journal of Glaciology, 5, 467–477, https://doi.org/10.3189/s002214300001844x, 1965.

Haas, C.: Late-summer sea ice thickness variability in the Arctic Transpolar Drift 1991-2001 derived from ground-based electromagnetic sounding, Geophysical Research Letters, 31, L09 402, https://doi.org/10.1029/2003GL019394, 2004.

Haas, C., Langhorne, P. J., Rack, W., Leonard, G. H., Brett, G. M., Price, D., Beckers, J. F., and Gough, A. J.: Airborne mapping of the sub-ice platelet layer under fast ice in McMurdo Sound, Antarctica, Cryosphere, 15, 247–264, https://doi.org/10.5194/tc-15-247-2021, 2021.

Hao, D., Bisht, G., Huang, M., Ma, P. L., Tesfa, T., Lee, W. L., Gu, Y., and Leung, L. R.: Impacts of Sub-Grid Topographic Representations on Surface Energy Balance and Boundary Conditions in the E3SM Land Model: A Case Study in Sierra Nevada, Journal of Advances in Modeling Earth Systems, 14, e2021MS002 862, https://doi.org/10.1029/2021MS002862, 2022.

Itkin, P., Hendricks, S., Webster, M., von Albedyll, L., Arndt, S., Divine, D., Jaggi, M., Oggier, M., Raphael, I., Ricker, R., Rohde, J., Schneebeli, M., and Liston, G. E.: Sea ice and snow characteristics from year-long transects at the MOSAiC Central Observatory, Elementa, 11, 00 048, https://doi.org/10.1525/elementa.2022.00048, 2023.

Kahn, B. H., Drouin, B. J., and L'ecuyer, T. S.: Assessment of sampling sufficiency for low-cost satellite missions: Application to prefire, Journal of Atmospheric and Oceanic Technology, 37, 2283–2298, https://doi.org/10.1175/JTECH-D-20-0023.1, 2020.

Landrum, L. L. and Holland, M. M.: Influences of changing sea ice and snow thicknesses on simulated Arctic winter heat fluxes, Cryosphere, 16, 1483–1495, https://doi.org/10.5194/tc-16-1483-2022, 2022.

Langhorne, P. J., Hughes, K. G., Gough, A. J., Smith, I. J., Williams, M. J., Robinson, N. J., Stevens, C. L., Rack, W., Price, D., Leonard, G. H., Mahoney, A. R., Haas, C., and Haskell, T. G.: Observed platelet ice distributions in Antarctic sea ice: An index for ocean-ice shelf heat flux, Geophysical Research Letters, 42, 5442–5451, https://doi.org/10.1002/2015GL064508, 2015.

Larue, F., Picard, G., Arnaud, L., Ollivier, I., Delcourt, C., Lamare, M., Tuzet, F., Revuelto, J., and Dumont, M.: Snow albedo sensitivity to macroscopic surface roughness using a new ray-tracing model, Cryosphere, 14, 1–26, https://doi.org/10.5194/tc-14-1651-2020, 2020.

Lawrence, I. R., Ridout, A. L., Shepherd, A., and Tilling, R.: A Simulation of Snow on Antarctic Sea Ice Based on Satellite Data and Climate Reanalyses, Journal of Geophysical Research: Oceans, 129, e2022JC019 002, https://doi.org/10.1029/2022JC019002, 2024.

https://doi.org/10.5194/egusphere-2025-1601
Preprint. Discussion started: 14 May 2025

Ledley, T. S. and Pfirman, S.: The impact of sediment-laden snow and sea ice in the Arctic on climate, Climatic Change, 37, 641–664, https://doi.org/10.1023/A:1005354912379, 1997.

Leonard, G. H., Turner, K. E., Richter, M. E., Whittaker, M. S., and Smith, I. J.: Brief communication: The anomalous winter 2019 sea-ice conditions in McMurdo Sound, Antarctica, Cryosphere, 15, 4999–5006, https://doi.org/10.5194/tc-15-4999-2021, 2021.

Light, B., Smith, M. M., Perovich, D. K., Webster, M. A., Holland, M. M., Linhardt, F., Raphael, I. A., Clemens-Sewall, D., Macfarlane, A. R., Anhaus, P., and Bailey, D. A.: Arctic sea ice albedo: Spectral composition, spatial heterogeneity, and temporal evolution observed during the MOSAiC drift, Elementa, 10, 000 103., https://doi.org/10.1525/elementa.2021.000103, 2022.

Lindsay, R. J. and Schweiger, A. H.: Arctic sea ice thickness loss determined using subsurface, aircraft, and satellite observations, Cryosphere, 9, 269–283, https://doi.org/10.5194/tc-9-269-2015, 2015.

Macfarlane, A. R., Löwe, H., Gimenes, L., Wagner, D. N., Dadic, R., Ottersberg, R., Hämmerle, S., and Schneebeli, M.: Thermal Conductivity of Snow on Arctic Sea Ice, EGUsphere, 83, 1–22, https://doi.org/10.5194/egusphere-2023-83, 2023.

Maksym, T. and Markus, T.: Antarctic sea ice thickness and snow-to-ice conversion from atmospheric reanalysis and passive microwave snow depth, Journal of Geophysical Research: Oceans, 113, C02S12, https://doi.org/10.1029/2006JC004085, 2008.

Malinowski, M. and Kwiecień, J.: A comparative study of Precise Point Positioning (PPP) accuracy using online services, Reports on Geodesy and Geoinformatics, 102, 15–31, https://doi.org/10.1515/rgg-2016-0025, 2016.

Manninen, T., Anttila, K., Jääskeläinen, E., Riihelä, A., Peltoniemi, J., Räisänen, P., Lahtinen, P., Siljamo, N., Thölix, L., Meinander, O., Kontu, A., Suokanerva, H., Pirazzini, R., Suomalainen, J., Hakala, T., Kaasalainen, S., Kaartinen, H., Kukko, A., Hautecoeur, O., and Roujean, J. L.: Effect of small-scale snow surface roughness on snow albedo and reflectance, Cryosphere, 15, 793–820, https://doi.org/10.5194/tc-15-793-2021, 2021.

Martin, J., Dadic, R., Anderson, B., Pirazzini, R., Vargo, L., Wigmore, O., and Horgan, H.: Snow On Antarctic Sea Ice - McMurdoSound 2022 - UAV Retrievals of Snow Topography and Snow Surface Temperature, https://doi.org/10.16904/envidat.634, 2025.

Massom, R. A. and Stammerjohn, S. E.: Antarctic sea ice change and variability - Physical and ecological implications, Polar Science, 4, 149–186, https://doi.org/10.1016/j.polar.2010.05.001, 2010.

Massom, R. A., Eicken, H., Haas, C., Jeffries, M. O., Drinkwater, M. R., Sturm, M., Worby, A. P., Wu, X., Lytle, V. I., Ushio, S., Morris, K., Reid, P. A., Warren, S. G., and Allison, I.: Snow on Antarctic sea ice, Reviews of Geophysics, 39, 413–445, https://doi.org/10.1029/2000RG000085, 2001.

Meredith, M., Sommerkorn, M., Cassotta, S., Ekaykin, A., Hollowed, A., Kofinas, G., Mackintosh, A., Melbourne-Thomas, J., Muelbert, M. M. C., Ottersen, G., Pritchard, H., and Schuur, E. A.: Intergovernmental Panel on Climate Change (IPCC). Polar Regions. In: The Ocean and Cryosphere in a Changing Climate: Special Report of the Intergovernmental Panel on Climate Change, IPCC, pp. 203–320, https://doi.org/10.1017/9781009157964.005, 2022.

Nicolaus, M., Hoppmann, M., Arndt, S., Hendricks, S., Katlein, C., Nicolaus, A., Rossmann, L., Schiller, M., and Schwegmann, S.: Snow Depth and Air Temperature Seasonality on Sea Ice Derived From Snow Buoy Measurements, Frontiers in Marine Science, 8, 1–21, https://doi.org/10.3389/fmars.2021.655446, 2021.

Nicolaus, M., Perovich, D. K., Spreen, G., Granskog, M. A., von Albedyll, L., Angelopoulos, M., Anhaus, P., Arndt, S., Jakob Belter, H., Bessonov, V., Birnbaum, G., Brauchle, J., Calmer, R., Cardellach, E., Cheng, B., Clemens-Sewall, D., Dadic, R., Damm, E., de Boer, G., Demir, O., Dethloff, K., Divine, D. V., Fong, A. A., Fons, S., Frey, M. M., Fuchs, N., Gabarró, C., Gerland, S., Goessling, H. F., Gradinger, R., Haapala, J., Haas, C., Hamilton, J., Hannula, H. R., Hendricks, S., Herber, A., Heuzé, C., Hoppmann, M., Høyland, K. V., Huntemann, M., Hutchings, J. K., Hwang, B., Itkin, P., Jacobi, H. W., Jaggi, M., Jutila, A., Kaleschke, L., Katlein, C.,

https://doi.org/10.5194/egusphere-2025-1601
Preprint. Discussion started: 14 May 2025

Kolabutin, N., Krampe, D., Kristensen, S. S., Krumpen, T., Kurtz, N., Lampert, A., Lange, B. A., Lei, R., Light, B., Linhardt, F., Liston, G. E., Loose, B., Macfarlane, A. R., Mahmud, M., Matero, I. O., Maus, S., Morgenstern, A., Naderpour, R., Nandan, V., Niubom, A., Oggier, M., Oppelt, N., Pätzold, F., Perron, C., Petrovsky, T., Pirazzini, R., Polashenski, C., Rabe, B., Raphael, I. A., Regnery, J., Rex, M., Ricker, R., Riemann-Campe, K., Rinke, A., Rohde, J., Salganik, E., Scharien, R. K., Schiller, M., Schneebeli, M., Semmling, M., Shimanchuk, E., Shupe, M. D., Smith, M. M., Smolyanitsky, V., Sokolov, V., Stanton, T., Stroeve, J., Thielke, L., Timofeeva, A., Tonboe, R. T., Tavri, A., Tsamados, M., Wagner, D. N., Watkins, D., Webster, M., and Wendisch, M.: Overview of the MOSAiC expedition: Snow and sea ice, Elementa: Science of the Anthropocene, 10, 000–046, https://doi.org/10.1525/elementa.2021.000046, 2022.

Orheim, O.: Surface snow metamorphosis on the Antarctic Plateau, in: Norsk Polarinstitutt. Årbok 1966, pp. 84–91, Norsk Polarinstitutt, Oslo, https://brage.npolar.no/npolar-xmlui/handle/11250/172819, 1968.

Parkinson, C. L.: Global sea ice coverage from satellite data: Annual cycle and 35-yr trends, Journal of Climate, 27, 9377–9382, https://doi.org/10.1175/JCLI-D-14-00605.1, 2014.

Pereyra Irujo, G.: IRimage: open source software for processing images from infrared thermal cameras, PeerJ Computer Science, 8, e977, https://doi.org/10.7717/peerj-cs.977, 2022.

Perovich, D. K. and Polashenski, C.: Albedo evolution of seasonal Arctic sea ice, Geophysical Research Letters, 39, L08 501, https://doi.org/10.1029/2012GL051432, 2012.

Perovich, D. K., Light, B., Eicken, H., Jones, K. F., Runciman, K., and Nghiem, S. V.: Increasing solar heating of the Arctic Ocean and adjacent seas, 1979-2005: Attribution and role in the ice-albedo feedback, Geophysical Research Letters, 34, L19 505, https://doi.org/10.1029/2007GL031480, 2007.

Picard, G., Dumont, M., Lamare, M., Tuzet, F., Larue, F., Pirazzini, R., and Arnaud, L.: Spectral albedo measurements over snow-covered slopes: Theory and slope effect corrections, Cryosphere, 14, 1497–1517, https://doi.org/10.5194/tc-14-1497-2020, 2020.

Pirazzini, R., David Brus, H.-R. H., Dadic, R., and Scnheebeli, M.: Drone-based sea ice albedo measurements and photogrammetry during the Arctic freeze-up in the MOSAiC expedition, https://doi.org/10.5194/EGUSPHERE-EGU21-11377, 2021.

Price, D., Rack, W., Haas, C., Langhorne, P. J., and Marsh, O.: Sea ice freeboard in McMurdo Sound, Antarctica, derived by surface-validated ICESat laser altimeter data, Journal of Geophysical Research: Oceans, 118, 3634–3651, https://doi.org/10.1002/jgrc.20266, 2013.

Price, D., Soltanzadeh, I., Rack, W., and Dale, E.: Snow-driven uncertainty in cryosat-2-derived antarctic sea ice thickness - Insights from McMurdo sound, Cryosphere, 13, 1409–1422, https://doi.org/10.5194/tc-13-1409-2019, 2019.

Réveillet, M., Dumont, M., Gascoin, S., Lafaysse, M., Nabat, P., Ribes, A., Nheili, R., Tuzet, F., Ménégoz, M., Morin, S., Picard, G., and Ginoux, P.: Black carbon and dust alter the response of mountain snow cover under climate change, Nature Communications, 13, 5279, https://doi.org/10.1038/s41467-022-32501-y, 2022.

Ricker, R., Fons, S., Jutila, A., Hutter, N., Duncan, K., Farrell, S. L., Kurtz, N. T., and Fredensborg Hansen, R. M.: Linking scales of sea ice surface topography: evaluation of ICESat-2 measurements with coincident helicopter laser scanning during MOSAiC, Cryosphere, 17, 1411–1429, https://doi.org/10.5194/tc-17-1411-2023, 2023.

Riihelä, A., Bright, R. M., and Anttila, K.: Recent strengthening of snow and ice albedo feedback driven by Antarctic sea-ice loss, Nature Geoscience, 14, 832–836, https://doi.org/10.1038/s41561-021-00841-x, 2021.

Román, A., Navarro, G., Tovar-Sánchez, A., Zarandona, P., Roque-Atienza, D., and Barbero, L.: ShetlandsUAVmetry: unmanned aerial vehicle-based photogrammetric dataset for Antarctic environmental research, Scientific Data, 11, 2052–4463, https://doi.org/10.1038/s41597-024-03045-1, 2024.

https://doi.org/10.5194/egusphere-2025-1601
Preprint. Discussion started: 14 May 2025

Rublee, E., Rabaud, V., Konolige, K., and Bradski, G.: ORB: An efficient alternative to SIFT or SURF, in: 2011 International Conference on Computer Vision, pp. 2564–2571, IEEE, https://doi.org/10.1109/ICCV.2011.6126544, 2011.

Simmonds, I.: Comparing and contrasting the behaviour of Arctic and Antarctic sea ice over the 35 year period 1979-2013, Annals of Glaciology, 56, 18 – 28, https://doi.org/10.3189/2015AoG69A909, 2015.

Skiles, S. M. K., Flanner, M., Cook, J. M., Dumont, M., and Painter, T. H.: Radiative forcing by light-absorbing particles in snow, Nature Climate Change, 8, 964–971, https://doi.org/10.1038/s41558-018-0296-5, 2018.

Smith, M. M., Light, B., Macfarlane, A. R., Perovich, D. K., Holland, M. M., and Shupe, M. D.: Sensitivity of the Arctic Sea Ice Cover to the Summer Surface Scattering Layer, Geophysical Research Letters, 49, e2022GL098 349, https://doi.org/10.1029/2022GL098349, 2022.

Sproles, E. A., Mullen, A., Hendrikx, J., Gatebe, C., and Taylor, S.: Autonomous aerial vehicles (AAVS) as a tool for improving the spatial resolution of snow albedo measurements in mountainous regions, Hydrology, 7, 1–16, https://doi.org/10.3390/hydrology7030041, 2020.

Stein, K., Timmermann, A., Kwon, E. Y., and Friedrich, T.: Timing and magnitude of southern ocean sea ice/carbon cycle feedbacks, Proceedings of the National Academy of Sciences of the United States of America, 117, 4498–4504, https://doi.org/10.1073/pnas.1908670117, 2020.

Stuecker, M. F., Bitz, C. M., Armour, K. C., Proistosescu, C., Kang, S. M., Xie, S. P., Kim, D., McGregor, S., Zhang, W., Zhao, S., Cai, W., Dong, Y., and Jin, F. F.: Polar amplification dominated by local forcing and feedbacks, Nature Climate Change, 8, 1076–1081, https://doi.org/10.1038/s41558-018-0339-y, 2018.

Sturm, M. and Holmgren, J.: Effects of microtopography on texture, temperature and heat flow in Arctic and sub-Arctic snow, Annals of Glaciology, 19, 63–68, https://doi.org/10.3189/1994aog19-1-63-68, 1994.

Sturm, M. and Holmgren, J.: An automatic snow depth probe for field validation campaigns, Water Resources Research, 54, 9695–9701, https://doi.org/10.1029/2018WR023559, 2018.

Sturm, M. and Massom, R. A.: Snow in the sea ice system: Friend or foe?, in: Sea Ice, pp. 65–109, Wiley-Blackwell Publishing Ltd, 3. edn., https://doi.org/10.1002/9781118778371.ch3, 2016.

Sturm, M., Holmgren, J., Konig, M., and Morris, K.: The thermal conductivity of seasonal snow, Journal of Glaciology, 43, 26–41, https://doi.org/doi:10.3189/S0022143000002781, 1997.

Tan, A. E. C., Mcculloch, J., Rack, W., Platt, I., and Woodhead, I.: Radar measurements of snow depth over sea ice on an unmanned aerial vehicle, IEEE Transactions on Geoscience and Remote Sensing, 59, 1–8, https://doi.org/10.1109/TGRS.2020.3006182, 2021.

Tateyama, K., Shirasawa, K., Uto, S., Kawamura, T., Toyota, T., and Enomoto, H.: Standardization of electromagnetic-induction measurements of sea-ice thickness in polar and subpolar seas, Annals of Glaciology, 44, 240–246, https://doi.org/10.3189/172756406781811484, 2006.

Tuzet, F., Dumont, M., Arnaud, L., Voisin, D., Lamare, M., Larue, F., Revuelto, J., and Picard, G.: Influence of light-absorbing particles on snow spectral irradiance profiles, Cryosphere, 13, 2169–2187, https://doi.org/10.5194/tc-13-2169-2019, 2019.

Wang, J., Luo, H., Yang, Q., Liu, J., Shi, Q., Han, B., Luo, H., Yang, Q. H., Liu, J. P., Yu, L. J., Shi, Q., and Han, B.: An unprecedented record low antarctic sea-ice extent during austral summer 2022, Advances in Atmospheric Sciences, 39, 1591–1597, https://doi.org/10.1007/s00376, 2022.

Warren, S. G. and Wiscombe, W. J.: A model for the spectral albedo of snow. II: snow containing atmospheric aerosols., Journal of the Atmospheric Sciences, 37, 2734–2745, https://doi.org/10.1175/1520-0469(1980)037<2734:AMFTSA>2.0.CO;2, 1980.

https://doi.org/10.5194/egusphere-2025-1601
Preprint. Discussion started: 14 May 2025

Webster, M., Gerland, S., Holland, M., Hunke, E., Kwok, R., Lecomte, O., Massom, R., Perovich, D., and Sturm, M.: Snow in the changing sea-ice systems, Nature Climate Change, 8, 946–953, https://doi.org/10.1038/s41558-018-0286-7, 2018.

Weller, G.: The Heat and Mass Balance of Snow Dunes on the Central Antarctic Plateau, Journal of Glaciology, 8, 277–284, https://doi.org/10.3189/s0022143000031257, 1969.

Wever, N., Leonard, K., Maksym, T., White, S., Proksch, M., and Lenaerts, J. T.: Spatially distributed simulations of the effect of snow on mass balance and flooding of Antarctic sea ice, Journal of Glaciology, 67, 1055–1073, https://doi.org/10.1017/jog.2021.54, 2021.

Wigmore, O. and Molotch, N. P.: Weekly high-resolution multi-spectral and thermal uncrewed-aerial-system mapping of an alpine catchment during summer snowmelt, Niwot Ridge, Colorado, Earth System Science Data, 15, 1733–1747, https://doi.org/10.5194/essd-15-1733-2023, 2023.

Wigmore, O., Mark, B., McKenzie, J., Baraer, M., and Lautz, L.: Sub-metre mapping of surface soil moisture in proglacial valleys of the tropical Andes using a multispectral unmanned aerial vehicle, Remote Sensing of Environment, 222, 104–118, https://doi.org/10.1016/j.rse.2018.12.024, 2019.

Wiscombe, W. J. and Warren, S. G.: A model for the spectral albedo of snow. I: pure snow., Journal of the Atmospheric Sciences, 37, 2712–2733, https://doi.org/10.1175/1520-0469(1980)037<2712:AMFTSA>2.0.CO;2, 1980.

Zatko, M. C. and Warren, S. C.: East Antarctic sea ice in spring: Spectral albedo of snow, nilas, frost flowers and slush, and light-absorbing impurities in snow, Annals of Glaciology, 56, 53 – 64, https://doi.org/10.3189/2015AoG69A574, 2015.

Zhou, X., Li, S., and Morris, K.: Measurement of all-wave and spectral albedos of snow-covered summer sea ice in the Ross Sea, Antarctica, Annals of Glaciology, 33, 267–274, https://doi.org/10.3189/172756401781818743, 2001.